The LABOCA survey of the Extended Chandra Deep Field South: Two modes of star formation in AGN hosts?

D. Lutz[1], V. Mainieri[2], D. Rafferty[3], L. Shao[1], G. Hasinger[4], A. Weiß[5], F. Walter[6], I. Smail[7], D.M. Alexander[8], W.N. Brandt[3], S. Chapman[9], K. Coppin[7], N.M. Förster Schreiber[1], E. Gawiser[10], R. Genzel[1], T.R. Greve[6], R.J. Ivison[11,12], A.M. Koekemoer[13], P. Kurczynski[10], K.M. Menten[5], R. Nordon[1], P. Popesso[1], E. Schinnerer[6], J.D. Silverman[14], J. Wardlow[8], Y.Q. Xue[3]

ABSTRACT

We study the co-existence of star formation and AGN activity in *Chandra* X-ray selected AGN by analyzing stacked 870μm submm emission from a deep

[1]Max-Planck-Institut für extraterrestrische Physik, Postfach 1312, 85741 Garching, Germany
lutz@mpe.mpg.de

[2]European Southern Observatory, Karl-Schwarzschild-Straße 2, 85748 Garching, Germany

[3]Department of Astronomy and Astrophysics, 525 Davey Lab, Pennsylvania State University, University Park, PA 16802, USA

[4]Max-Planck-Institut für Plasmaphysik, Boltzmannstraße 2, 85748 Garching, Germany

[5]Max-Planck-Institut für Radiastronomie, Auf dem Hügel 69, 53121 Bonn, Germany

[6]Max-Planck-Institut für Astronomie, Königstuhl 17, 69117 Heidelberg, Germany

[7]Institute for Computational Cosmology, Durham University, South Road, Durham, DH1 3LE, UK

[8]Department of Physics, Durham University, South Road, Durham, DH1 3LE, UK

[9]Institute of Astronomy, Madingley Road, Cambridge, CB3 0HA, U.K.

[10]Physics & Astronomy Department, Rutgers University, Piscataway, NJ 08854, USA

[11]SUPA, Institute for Astronomy, University of Edinburgh, Royal Observatory, Blackford Hill, Edinburgh, EH9 3HJ, UK

[12]UK Astronomy Technology Centre, Royal Observatory, Blackford Hill, Edinburgh, EH9 3HJ, UK

[13]Space Telescope Science Institute, 3700 San Martin Drive, Baltimore, MD 21218, USA

[14]Institute for the Physics and Mathematics of the Universe (IPMU), University of Tokyo, Kashiwanoha 5-1-5, Kashiwa, Chiba 277-8568, Japan

and wide map of the Extended Chandra Deep Field South, obtained with the LABOCA instrument at the APEX telescope. The total X-ray sample of 895 sources with median redshift z$\sim$1 drawn from the combined (E)CDFS X-ray catalogs is detected at $> 11\sigma$ significance at a mean submm flux of 0.49 ± 0.04mJy, corresponding to a typical star formation rate around $30 M_\odot \mathrm{yr}^{-1}$ for a T=35K, β=1.5 greybody far-infrared spectral energy distribution. The good signal to noise ratio permits stacking analyses for major subgroups, splitting the sample by redshift, intrinsic luminosity, and AGN obscuration properties. We observe a trend of star formation rate increasing with redshift. An increase of star formation rate with AGN luminosity is indicated at the highest $L_{2-10keV} \gtrsim 10^{44}\mathrm{erg\,s}^{-1}$ luminosities only. Increasing trends with X-ray obscuration as expected in some AGN evolutionary scenarios are not observed for the bulk of the X-ray AGN sample but may be present for the highest intrinsic luminosity objects with $L_{2-10keV} \gtrsim 10^{44}\mathrm{erg\,s}^{-1}$. This behaviour suggests a transition between two modes in the coexistence of AGN activity and star formation. For the bulk of the sample, the X-ray luminosity and obscuration of the AGN are not intimately linked to the global star formation rate of their hosts. The hosts are likely massive and forming stars secularly, at rates similar to the pervasive star formation seen in massive galaxies without an AGN at similar redshifts. In these systems, star formation is not linked to a specific state of the AGN and the period of moderately luminous AGN activity may not highlight a major evolutionary transition of the galaxy. The change indicated towards more intense star formation, and a more pronounced increase in star formation rates between unobscured and obscured AGN reported in the literature at highest ($L_{2-10keV} \gtrsim 10^{44}\mathrm{erg\,s}^{-1}$) luminosities suggests that these luminous AGN follow an evolutionary path on which obscured AGN activity and intense star formation are linked, possibly via merging. Comparison to local hard X-ray selected AGN supports this interpretation. Star formation rates in the hosts of moderate luminosity AGN at z$\sim$1 are an order of magnitude higher than at z$\sim$0, following the increase in the non-AGN massive galaxy population. At high AGN luminosities, hosts on the evolutionary link/merger path emerge from this secular level of star formation.

Subject headings: galaxies: active, galaxies: starburst, infrared: galaxies

1. Introduction

Observing the co-evolution of active galactic nuclei (AGN) and their hosts is key to understanding the similar cosmic evolution of the space density of luminous AGN and of the star formation rate density. This co-evolution also has to lead to today's fossil relations between remnant supermassive black hole mass and the properties of the host spheroid. Directly measuring the star formation rate of a high redshift galaxy is however particularly difficult for AGN hosts, since the AGN proper will disturb and overwhelm the rest frame UV and optical spectral and photometric star formation tracers already at modest luminosities, unless the AGN is obscured. Furthermore, star formation in the host may be noticeably obscured in particular at high star formation rates approaching that of high-redshift ultraluminous infrared and submillimeter galaxies. Infrared observations can thus play an important role for these studies. One approach that has been successfully applied to high redshift AGN is to use the mid-infrared polycyclic aromatic hydrocarbon ('PAH') emission features which can be separated from the strong AGN mid-IR continuum emission by means of low resolution spectroscopy (e.g., Houck et al. 2005; Lutz et al. 2005). However, even with the superb spectroscopic sensitivity of the *Spitzer* Space Telescope, this approach is limited for high redshifts to modest sample sizes. Alternatively, observations of the rest frame far-infrared/submm continuum have been used since the advent of the first sensitive submm photometers to measure star formation via the far-infrared/submm continuum from the associated cool (T∼35K) dust. This rests on the submm continuum being due to star formation in the host galaxy, with star formation dominating over the AGN heated dust emission at these wavelengths for all but the highest ratios of AGN luminosity to star formation in the host. Such a star formation dominance in the submm is possible because of the steep decline of AGN dust emission towards far-infrared and submm wavelengths (e.g., Pier & Krolik 1992, and later torus models), while the SEDs of star forming galaxies have a pronounced far-infrared (FIR) peak. The assumption of star formation dominating the submm emission is supported by several types of observations. For NGC 1068, the AGN in the local universe for which current spatial resolution is sufficent to separate the AGN from the host in the far-infrared/submillimeter range, this assumption is directly supported by observations (Pier & Krolik 1993; Papadopoulos & Seaquist 1999; Le Floc'h et al. 2001). Note that NGC 1068 falls well into the range of AGN luminosities (intrinsic $L_{2-10keV} \sim 10^{43.5} \, \mathrm{erg \, s^{-1}}$, Colbert et al. 2002) and far-infrared luminosities ($L_{IR} \sim 10^{11.3} \, L_{\odot}$) of the AGN found in deep X-ray surveys, such as the (E)CDFS AGN that are discussed below. Recent *Spitzer* spectroscopic studies using the polycyclic aromatic hydrocarbon (PAH) emission features in comparison to the far-infrared/submm emission lend further support to this assumption, indicating that, at $L_{AGN}/L_{FIR} \sim 10$, the far-infrared emission of local QSOs as well as of mm-bright high redshift QSOs is dominated by star formation in the host (Schweitzer et al.

2006; Netzer et al. 2007; Lutz et al. 2008), plausibly fed by large reservoirs of molecular gas (e.g., Evans et al. 2001; Solomon & VandenBout 2005). Here, we study a sample that is at or below this ratio of AGN and star forming luminosities (§3.2). Our sample does not reach the extreme values as some of the most luminous but mm-faint high-z QSOs, for which the assignment of far-infrared emission to star formation is more uncertain (see discussion in Lutz et al. 2008). Our sample is X-ray selected and thus not biased towards extremely obscured infrared objects as, e.g., some local ULIRGs or high redshift dust-obscured galaxies (e.g., Houck et al. 2005), for which the AGN contribution to the far-infrared emission may be significant.

Measuring the submm emission and on its basis the star formation rate of AGN hosts thus plays an important role in constraining the evolution of AGNs. Such studies directly benefit from the improving depth and areal coverage of current submm surveys. Both, the study of local AGN and of the AGN/galaxy (co)evolution have lead to the suggestion of models in which intense star formation events and powerful AGN activity are physically linked and sequentially occur in a single object (e.g., Sanders et al. 1988; Fabian 1999; Granato et al. 2004; Hopkins et al. 2006), in a process closely linked to the hierarchical merging of galaxies in the universe. In a nutshell, galaxy interaction followed by merging with associated gas inflow may trigger a powerful burst of star formation and subsequently feed the central black hole(s) of the merger, to produce a luminous AGN. The AGN may then quench the star formation event and shed the obscuring dust, and finally emerge as an optically visible QSO. In this evolutionary picture, an obscured AGN would sample the earlier phases of the AGN activity and would be associated with more powerful star formation in the AGN host, and thus stronger submm emission. As already implied by the typically non-merger morphology of local moderate-luminosity AGN (Seyferts), such an evolutionary picture may not always apply and its applicability needs to be studied as a function of AGN luminosity and redshift.

A different behaviour would be expected in the context of the successful unified picture of active galactic nuclei proper, in which the differences between obscured and unobscured types of AGN are the consequences of different viewing directions on intrinsically identically structured systems. In fact, for the AGN and its immediate dusty surroundings, for example in the form of a 'torus', emission would be expected to be equally strong or stronger in the face-on/unobscured direction compared to the edge-on direction, even at long far-infrared or submm wavelengths (e.g., Pier & Krolik 1992; Nenkova et al. 2008). However, because of the intrinsically weaker AGN/torus emission at far-infrared and submm wavelengths, such differences will be easily washed out by even a modest amount of star formation in the host galaxy. This would lead to the expectation of little dependency of submm emission to obscuration in the unified AGN picture. This 'unified' view is by no means contradictory to

the evolutionary picture. Considering both these perspectives only stresses that differences in submm emission found between different AGN types will to a large extent reflect evolutionary coupling of periods of AGN activity and host star formation, rather than AGN physics and orientation alone. If evolutionary signatures are found in the submm, the underlying mechanisms like merging have to be clarified from additional information like morphology or dynamics. Combining evolutionary and unified perspectives also emphasizes the need to separately test for possible evolutionary effects in populations of high redshift AGN of different luminosities, that may follow different paths of AGN and host evolution.

First looks at the submm emission of X-ray selected AGN have compared deep X-ray surveys to the first generation of (sub)mm surveys (e.g., Fabian et al. 2000; Severgnini et al. 2000; Hornschemeier et al. 2000; Barger et al. 2001; Almaini et al. 2003; Waskett et al. 2003). In general, no straightforward correspondence between typical sources from these X-ray surveys and bright submm sources detected with SCUBA (Holland et al. 1999) was established, and the average flux from submm stacking experiments of X-ray AGN was found to be low, e.g., $S_{850\mu m} = 1.21 \pm 0.27$mJy for the Chandra Deep field North (CDFN) (Barger et al. 2001) and $S_{850\mu m} = 0.48 \pm 0.27$mJy from the Canada-UK deep SCUBA survey (CUDSS) (Waskett et al. 2003), with insufficient S/N of the stacks for an in-depth analysis as a function of AGN properties. Pointed submm followup of selected, e.g., hard/luminous sources from the deep X-ray surveys resulted in a few detections (e.g., Mainieri et al. 2005; Rigopoulou et al. 2009) but also some upper limits. Conversely, SCUBA sources were often found to be associated with X-ray faint AGN in the very deepest X-ray surveys (Alexander et al. 2005a,b). These faint AGN do not dominate the energetics of the SCUBA sources and were undetectable in earlier analyses that were not based on the ultradeep 2Ms *Chandra* data. Their black hole masses appear modest compared to similarly massive galaxies and to more powerful AGN (Borys et al. 2005; alexander et al. 2008).

The study that has been perhaps most successful so far in establishing bright submm emission for an X-ray selected AGN population and finding trends with AGN properties used a different approach. Selecting luminous X-ray absorbed but optically bright AGN not from deep field *Chandra* or *XMM* X-ray survey data but from identification of X-ray brighter sources from the *ROSAT* survey, Page et al. (2001) were able to detect 4 of 8 X-ray absorbed QSOs at $S_{850\mu m} > 5$mJy. Later comparisons with matched X-ray unabsorbed samples (Page et al. 2004; Stevens et al. 2005) provided evidence for a lower submm detection rate of the X-ray unabsorbed objects. This difference in submm brightness between obscured and unobscured objects supports the evolutionary view, but questions remain in particular when comparing the large submm fluxes for some of the Page et al. (2001) objects with the more modest success of submm follow up observations of luminous hard sources from deep fields. If submm emission follows the emission at other wavelengths, this might

simply reflect the brighter observed fluxes and larger AGN luminosities of the Page et al. (2001) sources. However, it should be noted that these are selected as moderately X-ray obscured ($N_H \sim 10^{22} \mathrm{cm}^{-2}$) but optically unobscured (optical broad emission line = Type 1) AGN, unlike many of the heavily obscured AGN from deep X-ray fields, which show Type 2 optical spectra lacking broad lines. Like the broad lines, their bright optical magnitudes (Page et al. 2001b) argue against a significant obscuration of the AGN in the rest frame optical/UV. Extending such studies to include more typical obscured AGN is clearly important and a main motivation of this paper.

We here present a study of the submm properties of X-ray selected AGN in the (extended) Chandra Deep Field South (E)CDFS. Making use of a new submm map provided by LABOCA at the APEX facility (Weiß et al. 2009) as well as current X-ray data with substantially improved identification status and characterisation of the AGN, we can study the submm properties and hence host star formation rates as a function of AGN properties. Throughout the paper, we adopt an $\Omega_m = 0.3$, $\Omega_\Lambda = 0.7$ and $H_0 = 70$ $\mathrm{km\,s}^{-1}\,\mathrm{Mpc}^{-1}$ cosmology. When distinguishing between moderate luminosity (Seyfert) and high luminosity (QSO) AGN we refer to an intrinsic luminosity limit of $L_{2-10keV} = 10^{44} \mathrm{erg\,s}^{-1}$ unless stated otherwise.

2. Results from submillimeter mapping of the Extended Chandra Deep Field South

The excellent X-ray and multiwavelength coverage of the 0.1 square degree Chandra Deep Field South (CDFS) and the surrounding 0.3 square degree Extended Chandra Deep Field South (ECDFS), in combination with the powerful mapping capabilities of the LABOCA submm camera (Siringo et al. 2009) at the APEX telescope (Güsten et al. 2006), enables us to take a fresh look at the issues discussed in the introduction, making use of the improved observational resources. We use the LABOCA 870μm map obtained by the LESS (LABOCA ECDFS Submm Survey) consortium as described by Weiß et al. (2009). We use the beam-convolved v2.2 final map which includes a total of about 350 hours of observing time over an area of about $40' \times 40'$ with an rms noise level of about $1.2\,\mathrm{mJy\,beam}^{-1}$ in the inner $30' \times 30'$. This map and the catalog of 126 sources detected at $> 3.7\sigma$ is presented in Weiß et al. (2009). We also make use of the residual map obtained by subtracting these 126 sources, using fluxes that consider in a statistical sense the boosting by instrument and confusion noise (Weiß et al. 2009; Coppin et al. 2005).

2.1. Samples of X-ray AGN

To maximise the statistics and to allow us to draw meaningful conclusions for physically selected subgroups of X-ray selected AGN, we use X-ray based AGN samples from *Chandra* observations for both the ECDFS and the deeper but smaller CDFS, for a total of 895 X-ray sources. For the CDFS, we mainly use X-ray spectral properties of Tozzi et al. (2006) which are related to and based on the original CDFS observations of Giacconi et al. (2002). Recently, the deeper 2 Msec *Chandra* data and catalog for the CDFS have become available (Luo et al. 2008) but physical modelling comparable to the level of Tozzi et al. (2006) is not yet completed (Bauer et al., in preparation). We therefore use the updated 2 Msec observational data (observed fluxes, hardness ratios etc.), from Luo et al. (2008) where available but stick to the Tozzi et al. (2006) results for physical properties derived from X-ray spectral fitting (intrinsic luminosities, X-ray obscuring column density N_H, etc.). We have also added 94 CDFS sources that are new from Luo et al. (2008). Lacking X-ray spectral fitting, these were used only for the combined stack and when analysing properties as a function of redshift, no modelled properties are available for those. To reduce contamination by non-AGN sources we exclude here objects that are likely nearby normal/star forming galaxies. Discrimination between such objects and AGN is approximately possible by comparing their X-ray to their optical properties; specifically we have adopted a cutoff $log(f_X/f_R) \geq -1$ (e.g., Bauer et al. 2004), for the ratio of the X-ray flux to the optical R-band flux. Here we use as X-ray flux the observed full band flux if available, otherwise the larger of hard and soft band flux. For similar reasons, we exclude 14 sources from Tozzi et al. (2006) with intrinsic rest frame $L_{0.5-10keV} < 10^{41} \mathrm{erg\,s}^{-1}$. Sources with such low X-ray luminosities will mostly not be AGN (e.g., Bauer et al. 2004). We have furthermore excluded 20 sources from Tozzi et al. (2006) that are not re-detected in the deeper 2Msec data of Luo et al. (2008). In particular, this cut includes the Giacconi et al. (2002) XID 618. While this source, indicated in only one of two source extraction methods used by Giacconi et al. (2002), is coincident with an interesting z=4.76 submillimeter galaxy (SMG) (Coppin et al. 2009), its nature as an X-ray source is not confirmed by the deeper X-ray data of Luo et al. (2008). Including it in our analysis as a luminous obscured X-ray source as inferred by Tozzi et al. (2006) would increase the differences between luminous unobscured and obscured AGN that we discuss in Section 2.2. The overall CDFS list has 396 X-ray sources out of which 302 have X-ray spectral fitting from Tozzi et al. (2006).

For ECDFS sources outside of the CDFS, we use the X-ray catalog of Lehmer et al. (2005), supplemented with currently available identification and redshift information (Silverman et al. 2009, in preparation), but not yet including results of Treister et al. (2009). Again, we have imposed a $log(f_X/f_R) \geq -1$ cutoff to reduce contamination by non-AGN. We avoid double counting objects in the Lehmer et al. (2005) ECDFS catalog that are also

CDFS sources. Objects in the Giacconi et al. (2002) CDFS main catalog are identified by a flag in Lehmer et al. (2005). For these we use the CDFS data and spectral fitting only. The Luo et al. (2008) data detect more sources at the edge of the CDFS that are in the Lehmer et al. (2005) catalog but not flagged as also detected in the CDFS. We avoid double counting those by eliminating them via a 5″ radius match and using the ECDFS X-ray data.

For the CDFS sources of Tozzi et al. (2006) we adopt the positions provided in that paper. For the additional sources from Luo et al. (2008) we use their optical positions where given and X-ray positions otherwise. In the ECDFS, we use optical positions from identifications by Mainieri et al. (in preparation) when available and X-ray positions elsewhere. Note that the 27″ FWHM beam of the LABOCA map, obtained after convolution of the raw map with its own beamsize of 19.2″ (Weiß et al. 2009), is large compared to the *Chandra* X-ray positional uncertainities even for the least favourable case of modest S/N faint sources at large off-axis angles, reducing the need for optical identifications for the stacking process. Typically, *Chandra* X-ray positions are accurate to well below an arcsec (e.g., Fig. 5 of Luo et al. 2008).

We adopt as redshifts for all the CDFS sources of Tozzi et al. (2006) the values given in that paper. About half of these are spectroscopic redshifts from Szokoly et al. (2004) and other references, while the rest are photometric redshifts which benefit from the excellent multiwavelength coverage of the CDFS. For the ECDFS area and the identifications of Mainieri et al., we have used in order of preference (1) secure (e.g., two or more emission lines or clear spectral features, Ca H&K) spectroscopic redshifts from Silverman et al. (2009, in preparation), (2) other spectroscopic redshifts from the compilation of Rafferty et al. (2009, in preparation), (3) photometric redshifts derived by Rafferty et al. (2009, in preparation) from a comprehensive compilation of multi-band UV to *Spitzer*-IRAC photometry using the ZEBRA photo-z code and finally in a remaining 28 cases (4) photometric redshifts from the COMBO-17 survey which provides accurate photometric redshifts using photometry in 17 pass-bands from 350 to 930 nm. Here we have used the latest version of the COMBO-17 CDFS catalogue, following a calibration update (Wolf et al. 2008). We use this dataset with two limitations. We consider only COMBO-17 sources with R< 24 (Vega): at these magnitudes the errors on the photometric redshift estimates are expected to be less than $|z_{\rm phot} - z_{\rm spec}|/(1 + z_{\rm spec}) \approx 0.06$. The COMBO-17 data for galaxies fainter than R= 24 (Vega) are too shallow for accurate photo-z determination of AGN. Further, we limit the use of COMBO-17 photometric redshifts to z< 1.2 because at higher redshifts the COMBO-17 estimates become increasingly inaccurate due to the lack of NIR coverage (see Sec. 4.6 of Wolf et al. (2004)). We have waived this last constraint for objects best fitted with a QSO templates (MC_{class} = ′QSO′ in Wolf et al. (2004)) for which the photometric redshifts are accurate at least to z≈ 4 (see Fig. 18 of Wolf et al. (2004)). In total, we thus

have redshifts for about three quarters of the X-ray targets outside the CDFS. For the new Luo et al. (2008) sources we use redshifts from Rafferty et al. (2009, in preparation) where available.

The combined CDFS+ECDFS X-ray based catalog has 895 sources with a median X-ray flux of $3 \times 10^{-16} \mathrm{erg\,cm^{-2}\,s^{-1}}$ in the observed soft and $10^{-15} \mathrm{erg\,cm^{-2}\,s^{-1}}$ in the hard band. 748 sources have spectroscopic or reliable photometric redshifts in the range up to z~5 (median z=1.17), the median observed X-ray luminosity of those sources is $10^{43} \mathrm{erg\,s^{-1}}$. In the following we call this the 'combined' sample, while with 'CDFS' sample we designate the 302 sources from Tozzi et al. (2006) with X-ray spectral fits, remaining after the cuts described above (median z=1.04).

2.2. Stacking procedure

We derive average submm fluxes for a given source population by extracting both the map flux (in $\mathrm{Jy\,beam^{-1}}$) and the map rms noise, using bilinear interpolation to the source position in the beam-convolved LABOCA flux map and noise map. We then use the inverse variance weighted average of the fluxes measured over the stack.

Stacking procedures for data from large-beam deep submillimeter maps that are approaching the confusion limit at these wavelengths have to consider two effects. First, blank background and thus the 'zero point' of a sky image is hard to identify. At the RMS noise of ~1.2mJy of our data, integral number counts approach $10^4 \mathrm{deg^{-2}}$ (e.g., Coppin et al. 2006), which is only a modest factor away from the LABOCA beam density ($2 \times 10^4 \mathrm{deg^{-2}}$ for an area of $\pi\,HWHM^2$ of the convolved beam); see also the discussion in Weiß et al. (2009) on the contribution of confusion noise in the LABOCA map. This means there is effectively no clean background sky. Second, for the large submm beam an elevated signal at the position of a stacked source may originate from the wings of the beam of a nearby unrelated bright submm source. Chopped beam patterns would cause additional complications but do not apply to the scanned LABOCA data that were obtained in total power mode.

We have addressed this situation with simple Monte Carlo simulations, randomly placing $\sim 10^6$ Gaussian beams over a 1000×1000 pixel blank image and assuming a beam width (in pixels) equal to the LABOCA beam width. Input fluxes were distributed according to a simplified integral number count distribution with a power law slope -2 (approximating measurements of, e.g., Coppin et al. 2006; Weiß et al. 2009) and extending 3 orders of magnitude down from the brightest source in the map, deep into confusion. If the simulated image is offset to a mean value 0 and stacking experiments are done using the positions of subsets

of the input list, mean fluxes from stacks agree with the mean of the input fluxes within an error estimated from the standard deviation of the image, divided by the square root of the stacked sample size. The noise level of current submm maps and the fact that they do not reach below the knee of the integral counts implies a dynamic range between noise and brightest source of typically about an order of magnitude only. This reduces the effects of individual bright outliers on such error estimates. With a proper image zero point, the effects of the difficulty to define the background and of confusion thus cancel, and stacked fluxes can be used directly. In the LABOCA data, instrument noise is still (just) dominant over confusion noise (Weiß et al. 2009), its presence is again consistent with this stacking procedure. Fig. 1 shows the pixel flux histograms for the part of the LABOCA flux map that is within a factor 1.5 from the minimum RMS of $1.07 \, \mathrm{mJy \, beam^{-1}}$ and for the residual map after subtraction of detected sources (Weiß et al. 2009). In stacking experiments we subtracted the respective means ($0.154 \, \mathrm{mJy \, beam^{-1}}$ and $0.072 \, \mathrm{mJy \, beam^{-1}}$ for this part of the flux and residual map, respectively). This also ensures that zero average flux is returned from stacking random positions in the map. In deriving the stacked fluxes, we also calculate an inverse variance weighted stacked submap which, for stacks with significant detections, can be used to verify that the stacked beam is centered and reproduces the original beam of the map. Spatial clustering of the stacked population can in principle significantly affect source counts and stacking results. The effect on the stacks can be very important for instruments at similar wavelengths with much larger beams than that of APEX, like Planck-HFI (e.g., Negrello et al. 2005). It is negligible for the LABOCA beam at this wavelength (Bavouzet 2009), and hence not considered in our stacking.

We base our discussion on stacking the flux map but also provide stacking results for the residual map for comparison. In a few cases with poor statistics we explicitly discuss the effects of significant detections for the stacked population. Given the noticeable overlap between the submillimeter population and weak X-ray sources representing moderate luminosity AGN (e.g., Alexander et al. 2003, 2005b), exclusion of individually detected submm sources would bias our results. Future detailed identification campaigns and high spatial resolution submm followup of the LABOCA survey will allow supplementation of this statistical approach with one based on the confirmed nature of individual sources.

We quote below the stacked fluxes for various samples of ECDFS AGN. In assigning errors we consider that, while the instrument noise is gaussian to good approximation (Weiß et al. 2009), the pixel histogram of the LABOCA map is somewhat non-gaussian due to the effect of individually detected, as well as fainter, sources (Fig. 1). Positive detections in stacks are hence more likely than for purely gaussian noise. We provide in Tables 1 and 2 two error measures for the mean flux of each stack. For a sample with N sources, the error σ_{map} provides the standard deviation from comparing the mean fluxes of many (>1000)

samples of N sources each, drawn at random spatial positions in the map. The value of σ_{map} allows assessment of the significance of a stack's detection. The error $\sigma_{subsample}$ provides the standard deviation from comparing the mean fluxes of many subsamples of N sources each, drawn randomly from the fluxes measured at the positions of our combined sample of 895 AGN. This error is larger than σ_{map} since it also includes the spread in the properties of the AGN population. For that reason, we use it when assessing the significance of differences between subsamples of our overall AGN sample. We have also compared $\sigma_{subsample}$ to error estimates from bootstrapping into each subsample proper and found the latter estimates broadly consistent, but with large fluctuations due to the sometimes small subsamples that are used below.

2.3. Stacking results for different AGN samples

The stacked flux for the 895 X-ray sources from the combined CDFS+ECDFS sample is detected clearly at $S_{870\mu m}$=0.49±0.044mJy (11.1σ). The stacked image is shown in Fig. 2. A 2-dimensional gaussian fit to the stacked beam is centered at $2.2''\pm1.7''$ from the expected position and has a gaussian fit FWHM of $27'' \times 34''$ ($\pm3''$). These parameters support the correctness of the map reduction and the stacking procedure, given the nominal convolved beam of $27''$. Stacking the residual map after removal of all $> 3.7\sigma$ LABOCA point sources again provides a clear detection at $\sim70\%$ of this flux (Fig. 2, Table 1). Use of the residual map will lower the average flux of a stacked X-ray population by excluding members of that X-ray population that are individually detected SMGs. It can also lower the average flux if a subtracted point source is dominated by an unrelated object but includes a weaker submm flux that is originating from the blended X-ray source proper. Then, the flux at the position of the nearby X-ray source will be oversubtracted by removing a point source with the combined flux. This is related to one part of the 'boosting' effect on the fluxes of low S/N source detections from such a map. This is avoided for our residual map in a statistical sense because 'deboosted' (Coppin et al. 2005) fluxes for the detections have been used when deriving the residue (see also Weiß et al. 2009).

For redshift z$\sim$1, close to the median redshift of (E)CDFS AGN, and adopting a T=35K, β=1.5 greybody far-infrared continuum shape for the star formation powered part of the SED, the total infrared luminosity corresponding to our 0.49 mJy LABOCA detection is $\sim$ $2.6\times10^{11}L_\odot$. The inferred mean star formation rate is $\sim 27 M_\odot\,\mathrm{yr}^{-1}$, assuming star formation dominated submm emission, the conversion of Kennicutt (1998) and then multiplying by 0.6 to convert to a Chabrier (2003) initial mass function. Note that for z>0.5 and given the negative K correction for submm emission (e.g., Fig. 4 of Blain et al. 2002), the considerable

uncertainty of this estimate is mostly in the adopted temperature of dust heated by star formation (Factor $\lesssim 2$ in luminosity for a 5 K difference), rather than in the difference between individual source redshifts and the redshift z=1 adopted for the conversion. The average deep X-ray field AGN is thus residing in a moderately actively star-forming object, its luminosity placing it in the category usually called luminous infrared galaxies (LIRGs). This result certainly averages over a range of far-infrared luminosities but the LABOCA detection also in the stacked residual map argues that it is not only due to a few luminous outliers. Better characterizing this spread will be a task for the *Herschel* Space Observatory, the $\sim$10mJy far-infrared SED peak expected for the adopted greybody is well within its capabilities. Given the $> 11\sigma$ detection of the combined sample, stacks for subgroups can still be detectable at good significance. We use such substacks in the following to probe for trends with AGN properties.

We start with a simple splitting of the combined sample by redshift (see Table 1 for results of this and subsequent splittings of the combined sample). More than 80% of the sample have redshifts and are split into about equal groups below and above redshift z=1.2. There appears to be a trend towards higher star formation rates at higher redshift. A difference in mean submm flux between z<1.2 and z>1.2 sources is found at the 3.0σ level. As for other comparisons of AGN subsamples, we have adopted here the $\sigma_{subsample}$ errors from Tables 1 and 2. Comparing z<1.2 to z> 2 sources gives a similar difference but only at the 2.1σ level, due to the smaller size of the latter group. The sources without redshift assignment on average have slightly higher submm flux than any of these groups, consistent with the notion that a significant fraction of them are located at high redshift and remain more difficult to identify (Alexander et al. 2001; Mainieri et al. 2005a). We can also scrutinize this trend with redshift via a Spearman rank correlation test of the 746 individual submm fluxes with redshift measurements, rather than looking at binned averages. The correlation coefficient is a modest 0.108, not surprising given the significant noise on each individual flux measurement, but the probability of exceeding this coefficient in the null hypothesis of uncorrelated data is only 0.003. Interpreting trends of submm flux with redshift in terms of total infrared luminosity assumes their proportionality due to the negative K-correction. This assumption starts to fail at z$\lesssim$0.5. However, changes in the ratio of submm flux and inferred infrared luminosity are small at the median redshifts of the bins discussed here (Fig. 3). Deviations at z< 0.5 act in the direction of strengthening the trend of luminosity with redshift compared to the trend for submm flux. We illustrate this by reporting for those samples in Table 1 with complete redshifts also stacked IR luminosities, obtained from the luminosities of fiducial T=35K, β=1.5 greybodies matched to redshift and submm flux of each source. These stacked luminosities (see also lower panel of Fig. 3) thus capture the effect of the redshift distribution of the samples, and confirm its impact

to be small. Results from analysing redshift subgroups for the CDFS sample only, with its more complete identification status (see Table 2 for this and other results for this sample), agree with results for the combined sample in showing higher flux at higher redshift but with $< 2\sigma$ significance of the trends at the given sample sizes. Of course, the trends with redshift (see also Fig. 3) do not immediately imply evolution, because of the luminosity vs. redshift selection effects of the underlying X-ray surveys which are effectively flux limited.

To test this further, trends with X-ray luminosity need to be explored. Roughly half of those sources in the combined sample with redshifts are not used here, because of the lack of X-ray spectral modelling for many of the ECDFS-only sources. For them, only a simple observed X-ray luminosity can be computed from the distance and observed X-ray fluxes. No significant trends of average submm flux can be observed with this observed X-ray luminosity, but this could also be due to the effect of variations in the obscuring column density erasing trends with intrinsic AGN luminosity. This aspect is better addressed using only the CDFS sample, for which the spectral fits of Tozzi et al. (2006) assign an intrinsic rest frame hard X-ray (2-10 keV) luminosity for all sources including hard/obscured ones. We find no noticeable differences between groups or with respect to the total sample when dividing at $L_{2-10keV} = 10^{43}\mathrm{erg\,s^{-1}}$ into a more and a less luminous group with about half of the sample each (Table 2, Fig. 4). This changes at the most luminous end: Sources with $L_{2-10keV} > 10^{44}\mathrm{erg\,s^{-1}}$ have more than twice the average submm flux, and differ from the average of the CDFS sample at 2.2σ and from the sources with $L_{2-10keV} < 10^{44}\mathrm{erg\,s^{-1}}$ at 2.6σ. We further discuss this stronger star formation around the most luminous X-ray AGN below. Again the behaviour implied by the analysis of the stacks can be tested via a rank correlation of individual submm fluxes with $\log(L_{2-10keV})$. Given the upturn in submm only at the high X-ray luminosity end (Fig. 4) it is not suprising that no significant correlation is seen over the full range (N=302, C.C.=0.059, Significance 0.30), but correlation between submm flux and luminosity is found above $L_{2-10keV} > 10^{43.5}\mathrm{erg\,s^{-1}}$ (N=98, C.C.=0.26, Significance 0.01).

One of the most interesting parameters that is potentially linked by evolution to the level of star formation is the X-ray obscuring column density. Simple tests that can be done on the combined sample show no trend: Binning directly by X-ray hardness ratio as well as by crude estimates of the obscuring column density from the location in the redshift vs. hardness ratio diagram (e.g., Fig. 8 of Szokoly et al. 2004) does not show any noteworthy changes. We hence focus again on the CDFS sample using the modelled X-ray obscuring column densities N_H from Tozzi et al. (2006). As Table 2 and Fig. 5 show, there is no significant variation with obscuring column density even for this well-characterized sample and comparing subsamples that are individually detected at 3–5σ. We here split the sample at two different column densities. First, $N_H = 10^{22}\mathrm{cm^{-2}}$ is often used as the limit distinguishing unobscured AGN from the larger number of obscured AGN (e.g., Tozzi et al.

2006). As a second test we broke the sample at $N_H = 10^{23} \text{cm}^{-2}$ which would help identifying changes for the highest column density objects. These two cuts, as well as an intermediate one at $N_H = 3 \times 10^{22} \text{cm}^{-2}$ that gives roughly equally populated bins above and below the threshold, do not reveal any significant trends with X-ray obscuring column density. For the $N_H = 3 \times 10^{22} \text{cm}^{-2}$ cut which has the most equally distributed statistics, the ratio of stacked submm fluxes for sources more/less obscured than the cut is 1.1 ± 0.5, well below high ratios like the factor 4.4 found in the Stevens et al. (2005) comparison of obscured and unobscured very luminous QSOs. Using submm emission as star formation indicator, there hence seems to be no clear trend of host star formation with nuclear obscuration for the typical $L_{2-10keV} \sim 10^{43} \text{erg s}^{-1}$ AGN. Recent attempts using radio continuum emission (Rovilos et al. 2007) and the [OII]$\lambda 3727$ emission line (Silverman et al. 2009) to trace star formation agree in not finding such trends.

2.4. Results for the most luminous CDFS X-ray AGN

In the previous section, we have found for the full population of (E)CDFS X-ray AGN a trend of submm flux and star formation rate with redshift, a change with intrinsic X-ray luminosity only at the highest $L_{2-10keV} \geq 10^{44} \text{erg s}^{-1}$ AGN luminosities, the border that is conventionally adopted between 'AGN' and 'QSO', and no significant change with X-ray obscuring column density. We will discuss the implications below but first specifically repeat the check for possible trends with obscuration at the highest AGN luminosities. This is motivated by the large range of luminosities covered, combined with the possibility that evolutionary paths may significantly differ between luminous QSOs and lower luminosity AGN.

We first restrict the stacks which are formed via the Tozzi et al. (2006) obscuring column densities to AGN with high intrinsic luminosity $L_{2-10keV} \geq 3 \times 10^{43} \text{erg s}^{-1}$. A column density $N_H = 10^{23} \text{cm}^{-2}$ divides the sample roughly into half, but we also explore the traditional $N_H = 10^{22} \text{cm}^{-2}$ separation. In both cases the more obscured sources appear brighter in the submm (Table 2), but the difference stays well below 2σ significance in either case. As a next step toward the most luminous and reliable sources we further restrict to $L_{2-10keV} \geq 10^{44} \text{erg s}^{-1}$ and sources with spectroscopic redshifts (redshift quality ≥ 1 in Tozzi et al. (2006)). Again we find the more obscured sources to be submm brighter (Table 2, Fig. 5) with again a larger difference in submm flux if separating at $N_H = 10^{22} \text{cm}^{-2}$, but low significance. Such a change in mean star forming rate with obscuring column density occuring at roughly $N_H = 10^{22} \text{cm}^{-2}$ might indicate that the small variations with column density for the full CDFS sample may be dominated by the contribution of luminous AGN. Con-

sistent with this interpretation, a test splitting the less luminous $L_{2-10keV} < 3 \times 10^{43} \mathrm{erg\,s^{-1}}$ AGN at $N_H = 10^{22} \mathrm{cm^{-2}}$ further reduces the difference in submm flux between the two bins, compared to the full sample (Table 2).

An independent way of distinguishing unobscured from obscured AGN is the optical spectral classification. We use the highest luminosity AGN from Tozzi et al. (2006), for which either $L_{0.5-2keV}$ or $L_{2-10keV}$ is at least $10^{44} \mathrm{erg\,s^{-1}}$. Among those, we restrict ourselves to sources with spectroscopic redshift (redshift quality flag ≥ 1 in Tozzi et al. (2006)) and group them into optical Type 1 (BLAGN in the scheme of Szokoly et al. (2004), 10 sources[1]) or Type 2 (HEX, LEX or ABS classifications in the scheme of Szokoly et al. (2004), 17 sources[2]). Here we included XID 35 that was not classified by Szokoly et al. (2004) but for which an optical spectrum from the VVDS survey (Le Fevre et al. 2004) is lacking obvious broad lines. Consistent with the analysis where obscuration was defined via the X-ray obscuring column density, the obscured optical Type 2 AGN are again submm brighter (Table 2) than the unobscured Type 1 AGN, but the significance of the difference is low at just 1σ.

For both methods, the difference between submm fluxes of luminous unobscured and obscured AGN is stronger when stacking the flux map compared to stacking the residual map, suggesting a contribution of individually detected submm galaxies. Inspection shows that the 'hard' group defined by $N_H > 10^{22} \mathrm{cm^{-2}}$ or by optical Type 2 in both cases includes two X-ray sources with S/N in the submm map above 3 at their position, because they are close to submm sources that are detected at $> 3.7\sigma$. Both have extracted submm fluxes of $\gtrsim 6 \mathrm{mJy}$. The 'soft' group in contrast has no such sources. These two SMGs are near the X-ray sources with Giacconi et al. (2002) XIDs 51 (z=1.097) and 112 (z=2.940). We have investigated these associations on the LABOCA map, the VLA data of Miller et al. (2008) and the FIDEL $24\mu m$ image (M. Dickinson et al., in preparation). For XID 112, the position of the optical identification for which Szokoly et al. (2004) determined the redshift agrees within $1''$ with a weak $S_{1.4GHz} = 48\mu Jy$ radio source and a $24\mu m$ source, and is only $2.4''$ from SMG LESS J33152.0-275329 (Weiß et al. 2009). This supports the association despite the fact this is a relatively complex region of the LABOCA map with two more submm sources within less than 1 arcmin. For XID 52, again the optical position agrees with a $(93\mu Jy)$ radio source and a $24\mu m$ source, but the offset to LESS J33217.6-275230 is $10.8''$, large $(\gtrsim 2\sigma)$ for identifications of such a $\sim 5\sigma$ submm detection and the $27''$ convolved LABOCA beam

---

[1] Giacconi et al. (2002) XIDs 11, 22, 24, 42, 60, 62, 67, 68, 91, 206

[2] Giacconi et al. (2002) XIDs 18, 27, 31, 35, 45, 51, 57, 76, 112, 153, 156, 202, 253 (changed redshift from Szokoly et al. (2004) in Tozzi et al. (2006), see also Roche et al. (2006)), 263, 268, 547, 601

(e.g., equation B22 of Ivison et al. (2007) and the $6''$ positional accuracy estimated for the LABOCA map in Weiß et al. (2009)). We maintain this source in our stacks given that there is no nearby alternative radio identification for the SMG, and the region is again complex with the next SMG detection almost blended, but this association is clearly uncertain.

In our comparison of obscured and unobscured $L_{2-10keV} > 10^{44} \mathrm{erg\,s^{-1}}$ AGN we have found brighter submm fluxes by a factor $\sim$3 comparing X-ray column densities above to below $N_H = 10^{22} \mathrm{cm^{-2}}$ and by a factor $\sim$2 comparing optical Type 2 to Type 1. This is intriguing but the significance of the differences is too low in either case to claim a detection from our sample. The next steps in sample and field size and/or errors on the individual star forming rates will be needed for robustly confirming whether the stronger star formation reported at higher AGN luminosity in X-ray obscured vs. unobscured broad-line AGN (Page et al. 2001, and subsequent work) also holds in the regime of the brightest X-ray sources found in deep surveys like the (E)CDFS.

2.5. Results on individual literature X-ray sources

CXOCDFS J033229.9-275106 (also called CDFS-202; Norman et al. 2002) at redshift of z=3.70 has been considered a prototype of a luminous radio-quiet X-ray selected type 2 QSO. Sturm et al. (2006) have obtained a deep *Spitzer* mid-infrared spectrum of this source, detecting AGN continuum but not the 6.2μm rest wavelength PAH emission feature that could be detectable at this depth if the source were also hosting an extremely luminous SMG-like starburst. In accordance with this result, the LABOCA map does not show a detection at the position of CDF-S 202 ($S_{870} = -1.01 \pm 1.10$mJy).

From deep SCUBA follow up of four heavily X-ray absorbed and X-ray luminous AGN in the CDFS, Mainieri et al. (2005) report a $S_{850} = 4.8 \pm 1.1$mJy detection for the z=3.66 object CDFS-263. The LABOCA map gives a flux of $S_{870} = 1.88 \pm 1.16$mJy for this source. While we cannot support the Mainieri et al. (2005) result by an independent significant detection, the two measurements are still consistent within 2σ given the errors, and the source is likely among the submm brighter part of the X-ray AGN population. Rigopoulou et al. (2009) publish results from an extension of this project to 8 sources. They do not detect at 850μm CXOCDFS J033229.9-275106, consistent with the LABOCA and Spitzer results reported for this source above. Stacking their 8 targets in the LABOCA map we find $S_{870} = 1.55 \pm 0.41$mJy, consistent with results for $L_{2-10keV} > 10^{44} \mathrm{erg\,s^{-1}}$ Type 2 AGN reported above but somewhat lower than the $S_{870} = 4.0 \pm 0.5$mJy obtained from scaling the variance-weighted mean of the Rigopoulou et al. (2009) SCUBA results to 870μm.

Koekemoer et al. (2004) report the detection in the GOODS-S region of 7 'extreme X-ray/optical ratio sources' (EXOs) characterized by robust *Chandra* X-ray detections but optical nondetections to extremely low limits. All of these fall on the LABOCA map, none of them is individually detected and the stacked flux is 0.07±0.43mJy. While this nondetection at submm wavelengths excludes an explanation of EXOs by obscured AGN that are coexistent with extreme star formation, it is compatible with other possible spectral energy distributions of AGN at moderate to extremely high redshifts.

3. Discussion

Our data put strong limits on possible trends in submm brightness with obscuration for AGN with moderate luminosities, but are consistent with such a trend for luminous AGN. This result can be compared to previous studies. The first comparisons of deep X-ray and submm surveys mentioned in the introduction had too limited statistics to reliably address this issue. Page et al. (2001) used a different approach of selecting very luminous hard X-ray sources from the *ROSAT* survey and obtained significant submm detections in 4 out of 8 z=1–2.8 obscured AGN, the weighted mean submm flux for all eight is $S_{850} = 4.4 \pm 0.5$mJy. Subsequent papers (Page et al. 2004; Stevens et al. 2005) supported this result by matching to unobscured AGN of similar luminosity and redshift, and by extension of sample size, overall finding a ratio 4.4 in submm flux between X-ray unobscured and obscured AGN, and with the difference between submm detection rates of individual objects in the two groups significant at the 3-4σ level.

Our LABOCA results grouping luminous ($L_{2-10keV} > 10^{44}$erg s^{-1}) CDFS X-ray AGN by obscuration provide a ratio 2–3 in submm flux between obscured and unobscured objects, using separations by either $N_H = 10^{22}$cm^{-2} or by optical spectral type. However, due to the low significance we can not rule out neither absence of a difference nor trends as reported by Page et al. (2001) and subsequent papers. One should note that, considering the $\sim$8% correction from 870μm to 850μm flux densities for β=1.5 optically thin dust at z=1–4, our average submm fluxes of obscured sources are a factor $\sim$2-3 lower than reported by Page et al. (2001) and Stevens et al. (2005) for their samples. Assuming that the increase of submm flux with X-ray luminosity at highest luminosities (Fig. 4) continues beyond the range up to $L_{2-10keV} \sim 8 \times 10^{44}$erg s^{-1} covered by our sample, this difference may be due to the typically higher $L_{2-10KeV} \sim 10^{45}$erg s^{-1} luminosities of the Stevens et al. (2005) sample (see also Fig. 6). Observations with better statistics at $L_{2-10keV} \gtrsim 10^{44}$erg s^{-1} will be needed to firmly establish whether in this regime not only the observed increase in submm flux occurs, but also a gap starts to open between submm properties of unobscured and obscured

AGN.

An important point to note is that the Stevens et al. (2005) obscured QSOs are X-ray absorbed (though with typical N_H just above 10^{22}cm^{-2} not Compton thick) but optical broad line region (Type 1) objects. Stevens et al. are comparing optical Type 1 QSOs having low X-ray absorbing column density with Type 1 but higher X-ray absorbing column density. In contrast, we were first comparing groups defined by X-ray column density only, and in the second test comparing optical Type 1 to optical Type 2. Splitting our very small sample of 10 X-ray luminous BLAGN further by X-ray column density to fully reproduce the Stevens et al. (2005) approach did not show significant differences of subgroups in this group. While our result is consistent with the Stevens et al. (2005) finding of increased submm flux for obscured luminous AGN, the detailed role of different definitions of AGN obscuration remains to be investigated with better sensitivity and statistics.

Sturm et al. (2006) used *Spitzer* mid-infrared spectroscopy to detect or put limits on star formation in a sample of eight optical type 2 QSOs selected from deep X-ray surveys. These objects span a range of intrinsic luminosities $L_{0.5-10keV} = 10^{43.1}$ to 10^{45}erg s^{-1} and X-ray obscuring column densities $N_H = 10^{21.3}$ to $> 10^{24}$cm^{-2}, with all but one above 10^{22}cm^{-2}. We discussed the consistent LABOCA results for the z$\sim$3.7 source CDFS-202 above. For the major part of their sample, six sources at redshifts 0.205 to 1.38 (median $\sim$0.5), Sturm et al. (2006) report one detection and five limits on mid-infrared PAH emission with inferred star forming luminosities of the order $2 \times 10^{10}L_{\odot}$. This is lower than the $\sim 1.1 \times 10^{11}L_{\odot}$ obtained from the mean LABOCA flux for the z$<$1.2 redshift bin, averaging over all X-ray luminosities (Fig. 3), converting via our adoted T=35K, β=1.5 SED and assuming z=0.6. The Sturm et al. (2006) sample is small and may have missed star forming objects, but another factor likely contributing to the difference is the extrapolation from the PAH measurements to total star forming luminosity which is a function of interstellar medium conditions. Sturm et al. (2006) adopted a scaling factor based on the star forming galaxy M82. A scaling factor more similar to the one for high radiation field intensity environments, as suggested for star formation in hosts of local type 1 QSOs by Schweitzer et al. (2006), would increase the inferred star formation rates/limits of Sturm et al. (2006) by a factor $\sim$4 and bring them close to the typical z$<$1 star formation rate inferred from the LABOCA submm fluxes.

Another modestly sized z$\sim$0.5 QSO2 sample studied spectroscopically with *Spitzer* was presented by Zakamska et al. (2008). They observed 12 type 2 QSOs, 10 of which were selected from a large area SDSS sample primarily based on their optical Type 2 spectra, large [OIII] luminosities and bright mid-infrared continua. Two sources of their sample of 12 entered the sample from different far-infrared selected programs. Compared to the Sturm

et al. QSO2s they exhibit larger AGN mid-IR luminosities and, on the basis of X-ray to [OIII] ratios, possibly higher X-ray obscuring column densities. Zakamska et al. report PAH detections in 6 of 12 objects and infer a typical star formation luminosity of $\sim 5 \times 10^{11} L_\odot$ from the median of detections and limits. Both of these *Spitzer* spectroscopic studies are broadly consistent with the LIRG-like star forming luminosities of luminous type 2 AGN found in our LABOCA study. The overlap in luminosity, redshift and other properties is not large enough for a direct comparison of methods. A combination into a single analysis is not straightforward, given the different uncertainties that are involved in extrapolation to far-infrared luminosity from either the mid-infrared or submm side.

3.1. The co-evolution of X-ray survey AGN with their hosts: Two paths?

The differences expected in the merger evolution scenario between star formation around obscured and unobscured AGN may be present only at the high luminosity end of our sample and have been reported by Page et al. (2001) at yet higher luminosities. For the bulk of lower luminosity $L_{2-10keV} \sim 10^{43} \mathrm{erg\,s}^{-1}$ sources we do not observe any significant trend with obscuration. This is likely indicating a different evolutionary path for these AGN and their hosts.

The host properties of high-redshift Type 1 and luminous Type 2 AGN are difficult to constrain via common optical/near-infrared techniques, as the AGN often outshines the host. For the more accessible intermediate luminosity and Type 2 part of the population, several studies have concluded that $z \lesssim 1$ X-ray AGN are hosted by massive galaxies spanning the region from around the top of the 'blue cloud' via the 'green valley' to the 'red sequence' in a color - absolute magnitude diagram (Nandra et al. 2007; Silverman et al. 2008; Treister et al. 2009). These are luminous host galaxies, with few of them fainter than rest frame absolute magnitude $M_B = -20.5$ and typically brighter than $M_B = -21$ (see also Barger et al. 2003). Photometric stellar mass analyses for z∼1 X-ray AGN hosts (Alonso-Herrero et al. 2008; Bundy et al. 2008; Lehmer et al. 2008; Silverman et al. 2009) and analogy to the M_B – stellar mass relation for the general z=0.7-1 population (e.g., Cooper et al. 2008) suggests $\log(M^*) \gtrsim 10.5 M_\odot$ massive hosts. It is plausible from these results as well as from the local evidence (Kauffmann et al. 2003) to assume that also the bulk of the z∼1 unobscured/luminous X-ray AGN population resides in massive host galaxies.

Several studies have recently used mainly mid-infrared star formation indicators to conclude that typical massive galaxies at redshifts 0.7–2 are almost constantly forming stars at considerable star formation rates, with the stellar mass normalized 'specific star formation rate' (SSFR) increasing with redshift. This is concluded from the presence of a fairly tight

mass – SFR relation which shifts towards higher SSFR with redshift (Noeske et al. 2007; Elbaz et al. 2007; Daddi et al. 2007). The tightness of this relation suggests a high duty cycle of star formation. For massive z∼ 2 galaxies, a strong role of secular evolutionary processes compared to individual brief merger events is independently suggested by dynamical studies of rest frame optical/UV selected high redshift galaxies (e.g., Förster Schreiber et al. 2006; Genzel et al. 2008; Shapiro et al. 2008).

This developing picture of z∼1–2 galaxy evolution is naturally complemented by our results for the bulk of the X-ray sample: Strong trends of host star formation rate with AGN obscuration are lacking because such star formation rates are pervasive in galaxies of similar mass and redshift. The hosts are evolving secularly and star formation is not linked to a specific state of the AGN. The typical $\sim 30 M_\odot$ yr^{-1} estimated above for AGN hosts assuming star formation dominated submm emission compares well with typical star formation rates in z∼1 log(M*)∼10.5$M_\odot$ galaxies (Noeske et al. 2007; Daddi et al. 2007). A further comparative interpretation is currently not warranted given the uncertainty in the stellar masses of the AGN hosts and the fact that the comparison of star formation rates is subject to different extrapolation effects. Star formation rates in these studies are based on extrapolation from the optical/mid-infrared while we extrapolate from the submm. This mismatch can be partly remedied by a comparison to submm fluxes (measuring the rest frame far-infrared and indirectly star formation rates) that were estimated for optically selected galaxies from the LESS LABOCA survey. Greve et al. (2009) find for a K-selected K$_{Vega} \leq 20$ sample stacked 870μm fluxes of 0.17±0.01 mJy (z<1.4) and 0.47±0.03 mJy (z>1.4), similar but slightly below our trend for the AGN hosts, and again with a positive trend with redshift. The increase in AGN host star formation rate with redshift (Fig. 3) is combined with a relation SFR to AGN luminosity that is flat over a wide range of moderate AGN luminosities (Fig. 4), i.e. SFR does not depend on AGN luminosity. This is consistent with the moderate luminosity AGN hosts indeed following the increase of SSFR with redshift of the general galaxy population. Firmly establishing this behaviour will require studies with better SFR sensitivity for individual objects, removing the need to average over large stacks and better breaking redshift-luminosity correlations in the parent X-ray sample. Silverman et al. (2009) use the AGN-subtracted [OII]λ3727 emission line to compare star formation rates in 0.48 < z < 1.02 AGN and inactive galaxies of same stellar mass at same redshift. For moderate luminosity $42 < log(L_{0.5-10keV}) < 43.7$ they find indistinguishable SFR distributions in full agreement with the submm result. When including larger AGN luminosities a SFR excess is indicated in their data. If robust to the increasing technical difficulties of measuring mass and [OII] SFR for luminous AGN, this could indicate the onset of star formation enhancement due to e.g. merging.

Our interpretation that most of the moderate luminosity X-ray survey AGN are hosted

by massive secularly evolving galaxies is consistent with morphological analyses. *HST* studies of z∼1 X-ray AGN hosts (Grogin et al. 2005; Pierce et al. 2007) find the hosts to typically be bulge-dominated galaxies with only a modest fraction of hosts showing clear morphological evidence for recent major mergers, such as strong asymmetries.

Analysis of deep X-ray surveys has clearly shown a difference in the redshift evolution of high and lower luminosity AGN, with the comoving density of lower luminosity AGN peaking at lower redshift than the z∼2 'Quasar epoch'. Since cosmic halo merger evolution can be roughly matched to the evolution of quasars but not to the evolution of lower luminosity AGN, this has been interpreted in terms of a difference between merger driven accretion at high AGN luminosities and more secular evolution at lower luminosities (e.g., Hasinger 2008; Hopkins & Hernquist 2009, and references therein).

All these lines of evidence place the bulk of the AGN population detected in deep X-ray surveys on a relatively gentle and secular evolutionary path. In these sources, X-ray obscuration may vary through orientation of the immediate AGN environment in a classical unified/torus picture, and possibly also with an additional contribution by obscuration on larger host scales, but obscuration is not intimately linked to the global star formation rate of the host. Only for the $L_{2-10keV} \gtrsim 10^{44} \mathrm{erg\,s^{-1}}$ QSO-like AGN, obscuration may coincide with high star formation, consistent with a classical merger evolutionary path.

3.2. Star formation and AGN accretion rates

Over cosmic time, the growth and merger rates of black holes and their hosts have to establish the local black hole – bulge mass relation (e.g., Marconi & Hunt 2003; Häring & Rix 2004). In this context, it is interesting to compare for high redshift AGN populations the current accretion rate onto the black hole and the host growth via star formation with a relation that would establish on average the local ratio of black hole and bulge mass. Our results permit steps in this direction for X-ray selected AGN, within the constraints of results that are based on averaging over sizeable samples.

In Fig. 6 we show the location of the CDFS stacks, grouped by intrinsic 2–10keV X-ray luminosity as in Fig. 4, now in a diagram comparing star forming and AGN luminosity. To obtain the AGN luminosities we have converted from median 2-10keV X-ray luminosity for each luminosity bin, assumed to be AGN dominated, to monochromatic 5100Å luminosity using the luminosity-dependent α_{OX} relation of Steffen et al. (2006) as cast into units suitable for our purpose by Maiolino et al. (2007). We have then converted to AGN bolometric luminosity adopting $L_{Bol}=7\nu L_\nu(5100\text{Å})$ (e.g., Netzer & Trakhtenbrot 2007). The star form-

ing luminosities are based on the stacked greybody luminosities for an adopted T=35K, β=1.5 SED at the individual redshift of each source. For comparison, we add samples of low and high redshift QSOs (Netzer et al. 2007; Lutz et al. 2008; Page et al. 2004; Stevens et al. 2005; Priddey et al. 2003; Omont et al. 2003). The local universe ratio of black hole to bulge mass ratio of 0.14% (Häring & Rix 2004) can be converted into a formal 'steady growth luminosity ratio' for star formation and AGN L_{SF}/L_{AGN}=4.7(0.1/η) that is shown in Fig. 6 for a black hole accretion efficiency η=0.1.

The points shown for the CDFS X-ray AGN reflect the stack averages, i.e., the individual objects may scatter noticeably towards higher and lower star formation rates. Nevertheless, their location around the 'continuous growth' line is compatible with the picture of secular evolution outlined in the previous section. AGN accretion rates or star formation rates may here fluctuate to some extent with time, moving individual sources around this line in Fig. 6 in left/right and up/down direction, respectively, but the location of the population overall does not require to place them in any special evolutionary state that would be deviating from a long term growth. Only the highest luminosity $L_{2-10keV} > 10^{44}$erg s^{-1} CDFS AGN approach the location of the local and high redshift QSO in the comparison samples. Compared to the continuous growth ratio, these most luminous X-ray AGN as well as the QSOs are growing their black holes at a much faster rate, indicating that the matching star formation is most likely spread over longer timescales. Again, we find that only the most luminous CDFS AGN match the possibly merger related evolutionary pattern of QSOs.

The combination in Fig 6 of the CDFS AGN with the more luminous high redshift AGN observed in the (sub)mm by Priddey et al. (2003), Omont et al. (2003), Page et al. (2004) and Stevens et al. (2005) confirms the behaviour discussed in Sect. 2.1. Star formation in the hosts of modest luminosity high-z AGN seems to depend little on the exact AGN luminosity - reflecting the 'secular path'. These external samples, however, extend the increase in star formation above $L_{2-10keV} \sim 10^{44}$erg s^{-1}($L_{AGN} \sim 3 \times 10^{45}$erg s^{-1}) that was already indicated in the CDFS data - reflecting the connection between star formation and AGN on the 'evolutionary connection/merger path'. The combined results for these samples and the CDFS AGN can be approximated by a simple relation $L_{SF} = 10^{44.56} + 10^{27.7} \times L_{AGN}^{0.38}$ (dashed line in Fig. 6). Here, the smaller slope for the power law at high AGN luminosities compared to the slope 1 implied by the 'steady growth ratio' plausibly reflects that at the highest AGN luminosities the AGN growth (at the time of observation) is increasingly faster compared to the host growth. While this simple two component – constant plus power law – parametrization is a plausible reflection of the two growth modes, it should be considered illustrative and detailed parameters viewed with caution, given the sample selections and the fact that we here compare z~1 AGN at moderate luminosities and z~2 AGN at the highest luminosities.

3.3. Comparison to the local AGN population

The two evolutionary paths outlined above for high redshift AGN from deep X-ray fields imply a straightforward consistency check with the local AGN population. If the hosts of moderate luminosity AGN at z∼1 have star formation rates similar to nonactive massive galaxies at the same redshift, the star formation rates in the host of moderate luminosity AGN should follow the decrease of star formation on the general massive galaxy population towards redshift zero.

To perform this check in a methodology as consistent with the LABOCA analysis of (E)CDFS X-ray AGN as possible, we have used a local unbiased 14-150keV extremely hard X-ray selected AGN sample from the 39 month Palermo *Swift*-BAT catalog (PSB, Cusumano et al. 2009, see also Tueller et al. (2008) for an earlier BAT AGN catalog) in conjunction with the *IRAS* all-sky far-infrared survey. We selected (Shao et al., in preparation) from the PSB survey sources classified as Seyferts, LINERs, quasars, and other AGN, explicitly omitting blazars. We excluded remaining objects with the possibility of a strong nonthermal contribution to the far-infrared on the basis of the NED SED, objects at galactic latitude $|b| < 15$ and objects at redshift z>0.3 for which the *IRAS* 60μm band no longer probes the rest-frame far-infrared. For the remaining 293 AGN we used the *IRAS* Faint Source Catalog 60μm detections where available, otherwise we used Scanpi[3] to obtain 60μm measurements for faint or individually nondetected objects. We calculated rest frame 2–10keV luminosities extrapolating from the BAT fluxes and the redshift, assuming an AGN photon index of 1.8, and infrared luminosities $\nu L_\nu(60\mu$m) in the observed frame. Because about 20% of the sample are individually undetected at 60μm and for consistency with the LABOCA stacking, we stacked the luminosities in seven 2–10keV luminosity bins spanning the PSB luminosity range with sufficient statistics in each bin.

Star forming and AGN luminosities for these local AGN stacks are shown in Fig. 6 in direct comparison to the (E)CDFS results. At moderate AGN luminosities ($L_{AGN} < 3 \times 10^{44}$erg s^{-1}), the star forming luminosities of local hosts are about an order of magnitude lower than in z∼1 (E)CDFS AGN hosts. On the other hand, these local AGN appear to follow down to lower AGN luminosities the diagonal correlation of star forming and AGN luminosity that is reflecting the 'merger path'. This is in full agreement with previous local work, for example the infrared-based results of Rowan-Robinson (1995) and Netzer et al. (2007) covering the regime of local QSOs, and modelling based on SDSS spectroscopy by Netzer (2009). The latter traces a correlation down to even lower AGN luminosities $\lesssim 10^{43}$erg s^{-1} where star formation rates in our BAT stacks flatten out. We speculate this might relate

---

[3]http://scanpi.ipac.caltech.edu:9000/applications/Scanpi/index.html

to a more difficult disentanglement of weak AGN and moderately star forming galaxies galaxies in optical spectra than in very hard-X vs. far-infrared.

Mullaney et al. (2010) use *Spitzer* 70μm data to trace the evolution of the far-infrared to X-ray luminosity ratio of AGN to redshift z$\sim$2. They find no significant change of IR luminosity with redshift for luminous $L_{2-10keV} = 10^{43-44}$erg s^{-1} X-ray AGN but an increase for more modest $L_{2-10keV} = 10^{42-43}$erg s^{-1} AGN. While an observed wavelength of 70μm makes for a difficult AGN/host diagnostic at the high-z/high-l end of that range, where AGN heated dust will enter strongly the observed band, these results agree with our submm-based finding that an increase of host SFR from local towards z$\sim$1 occurs for modest luminosity AGN only. We note that the FIR luminosity increase by about an order of magnitude to z$\sim$1 would be difficult to reconcile with the alternative explanation of an AGN covering factor increase (Mullaney et al. 2010), since covering factors $<$0.1 would be required for local AGN. Another recent study (Trichas et al. 2009) addresses the starburst/AGN connection in luminous z$\sim$1 SWIRE AGN. Being based on rare 70μm detections only it is not directly comparable to our work but consistent with the presence of elevated star formation in $L_{2-10keV} \sim 10^{43}$erg s^{-1} z$\sim$ AGN.

Our finding of elevated star formation in modest luminosity high z AGN is consistent with the change of typical star formation rates from z$\sim$1 to z=0 in the non-active massive galaxy population (Noeske et al. 2007; Elbaz et al. 2007; Daddi et al. 2007). In Fig. 6, both local and z$\sim$1 AGN are consistent with a 'secular' path with star forming luminosity independent of AGN luminosity, and an 'evolutionary connection' path with increasing star forming luminosity at high AGN luminosity. The evolutionary path, possibly linked to merging, appears to emerge locally at lower AGN luminosities from the locally lower level of general star formation.

We have previously discussed the location of local and high redshift X-ray selected AGN and optical QSOs in the L_{SF} vs. L_{AGN} diagram of Fig. 6. In the merger evolutionary picture and in a sequence where the strongest star formation occurs before strongest AGN activity, galaxies should follow a loop path moving up in the L_{SF} vs. L_{AGN} diagram with the rise of star formation and then to the right and perhaps down towards the most intense AGN phase (see discussion in Netzer (2009)). We have placed SMGs *with weak X-ray AGN* from Alexander et al. (2005a) in Fig. 6 to show that their location in comparison to QSOs is consistent with such a path. SMGs without detected AGN would be found yet further to the left in Fig. 6. Comparing the location of individual submm-selected SMGs hosting weak AGN to the X-ray selected CDFS stacks has to be done with caution since the CDFS stacks themselves will contain similar SMGs contributing to the upturn in mm emission at high X-ray luminosity. A thorough analysis of possible evolutionary loops in such a L_{SF} vs. L_{AGN}

diagram will thus have to be done on the basis of future individual measurements for sources in all the relevant parts of the diagram.

4. Conclusions

We have used the combination of the LESS 870μm survey and deep X-ray surveys of the (E)CDFS region to study star formation in the hosts of AGN covering a wide range of redshifts and luminosities centered around z$\sim$1 and $L_{2-10keV} \sim 10^{43}$erg s^{-1}. Stacking LESS data at the positions of all 895 AGN we detect at high significance submm emission at $S_{870\mu m}$=0.49$\pm$0.04mJy corresponding to average star formation rates of about $30 M_{\odot}$ yr^{-1}. Using the good statistics to break down the sample according to AGN properties, we find an increase with redshift and little change with AGN luminosity, except for indications for an upturn in host star formation at $L_{2-10keV} > 10^{44}$erg s^{-1}. The bulk of the X-ray AGN do not show changes with AGN obscuration as expected from the merger evolutionary scenario, but such a behaviour may emerge at $L_{2-10keV} \gtrsim 10^{44}$erg s^{-1}.

Combined with results for higher luminosity AGN not properly sampled in the 0.25 square degree ECDFS, we conclude that the bulk of deep survey X-ray AGN seem to be hosted by galaxies evolving secularly, with star formation rates similar to comparably massive non-active galaxies and no close link between AGN and global host star formation. In contrast, the most luminous $L_{2-10keV} > 10^{44}$erg s^{-1} AGN seem to follow a path where AGN activity and obscuration appear to be more closely linked to host star formation, likely via merger evolution.

The properties of local *Swift*-BAT selected AGN with *IRAS*-based far-infrared star forming luminosities are consistent with these two paths. The host star formation rates of moderate luminosity AGN are decreasing from z$\sim$1 to z=0 similar to the decrease of SFR in non-active massive galaxies over this redshift interval.

REFERENCES

Alexander, D.M., Brandt, W.N., Hornschemeier, A.E., Garmire, G.P., Schneider, D.P., Bauer, F.E., Griffiths, R.E. 2001, AJ, 122, 2156

Alexander, D.M., et al. 2003, AJ, 125, 383

Alexander, D.M., Smail, I., Bauer, F.E, Chapman, S.C., Blain, A.W., Brandt, W.N., Ivison, R.J. 2005a, Nature, 434, 738

Alexander, D.M., Bauer, F.E., Chapman, S.C., Smail, I., Blain, A.W., Brandt, W.N., Ivison, R.J. 2005b, ApJ, 632, 736

Alexander, D.M., et al. 2008, AJ, 135, 1958

Almaini, O., et al. 2003, MNRAS, 338, 303

Alonso-Herrero, A., Pérez-González, P.G., Rieke, G.H., Alexander, D.M., Rigby, J.R., Papovich, C., Donley, J.L., Rigopoulou, D. 2008, ApJ, 677, 127

Barger, A.J., Cowie, L.L., Steffen, A.T., Hornschemeier, A.E., Brandt, W.N., Garmire, G.P. 2001, ApJ, 560, l23

Barger, A. et al. 2003, AJ, 126, 623

Bauer, F.E., et al. 2004, AJ, 128 ,2048

Bavouzet, N., 2009, Thèse de Doctorat, Université Paris Sud 11

Blain, A.W., Smail, I., Ivison, R.J., Kneib, J.-P., Frayer, D.T. 2002, Phys. Rep., 369, 111

Borys, C., Smail, I., Chapman, S.C., Blain, A.W., Alexander, D.M., Ivison, R.J. 2005, ApJ, 635, 853

Bundy, K., et al. 2008, ApJ, 681, 931

Chabrier, G. 2003, PASP, 115, 763

Colbert, E.J.M., Weaver, K.A., Krolik, J.H., Mulchaey, J.S., Mushotzsky, R.F. 2002, ApJ, 202, 581

Cooper M.C., et al. 2008, MNRAS, 383, 1058

Coppin, K., Halpern, M., Scott, D., Borys, C., Chapman, S. 2005, MNRAS, 357, 1022

Coppin, K., et al. 2006, MNRAS, 372, 1621

Coppin, K., et al. 2009, MNRAS, in press (arXiv 0902.4462)

Cusumano, G., 2009, AIP conference proceedings 1126, 104

Daddi, E., et al. 2007, ApJ, 670, 156

Elbaz, D., et al. 2007 A&A, 468, 33

Elvis, M., et al. 1994, ApJS, 95, 1

Evans, A.S, Frayer, D.T., Surace, J.A., Sanders, D.B. 2001, AJ, 121, 3286

Fabian, A.C. 1999, MNRAS, 308, L39

Fabian, A.C., et al. 2000, MNRAS, 315, L8

Förster Schreiber, N.M., et al. 2006, ApJ, 645, 1062

Genzel, R., et al. 2008, ApJ, 687, 59

Giacconi, R., et al. 2002, ApJS, 139, 369

Granato, G.L., de Zotti, G., Silva, L., Bressan, A., Danese, L. 2004, ApJ, 600, 580

Greve, T., et al. 2009, ApJ, submitted (arXiv:0904.0028)

Grogin, N.A., et al. 2005, ApJ, 627, L97

Güsten, R., Nyman, L.Å., Schilke, P., Menten, K., Cesarsky, C., Booth, R. 2006, A&A, 454, L13

Häring, N., Rix, H.W. 2004, ApJ, 604, L89

Hasinger, G., 2008, A&A, 490, 905

Holland, W.S., et al. 1999, MNRAS, 303, 659

Hopkins, P.F., Hernquist, L., Cox, T.J., Di Matteo, T., Robertson, B., Springel, V. 2006, ApJS, 163, 1

Hopkins, P.F., Hernquist, L. 2009, ApJ, 694, 599

Hornschemeier, A.E., et al. 2000, ApJ, 541, 49

Houck, J., et al. 2005, ApJ, 622, L105

Ivison, R.J., et al. 2007, MNRAS, 380, 199

Kauffmann, G., et al. 2003, MNRAS, 346, 1055

Kennicutt, R.C. 1998, ARA&A, 36, 189

Koekemoer, A., et al. 2004, ApJ, 600, L123

Lehmer, B.D., et al. 2005, ApJS, 161, 21

Lehmer, B.D., et al. 2008, ApJ, 681, 1163

Le Fevre, O., et al. 2004, A&A, 428, 1043

Le Floc'h, E., Mirabel, I.F., Laurent, O., Charmandaris, V., Gallais, P., Sauvage, M., Vigroux, L., Cesarsky, C. 2001, A&A, 367, 487

Luo, B., et al. 2008, ApJS, 179, 19

Lutz, D., et al. 2005, ApJ, 625, L83

Lutz, D., et al. 2008, ApJ, 684, 853

Maiolino, R., et al. 2007, A&A, 468, 979

Mainieri, V., et al. 2005, MNRAS, 356, 1571

Mainieri, V., et al. 2005a, A&A, 437, 805

Marconi, A., Hunt, L.K, 2003, ApJ, 689, L21

Miller, N., Fomalont, E.B., Kellermann, K.I., Mainieri, V., Norman, C., Padovani, P., Rosati, P., Tozzi, P. 2008, ApJS, 179, 114

Mullaney, J.R., Alexander, D.M., Huynh, M., Goulding A.D., Frayer, D. 2010, MNRAS, 401, 995

Nandra, K., et al. 2007, ApJ, 660, L11

Negrello, M., González-Nuevo, J., Magliochetti, M., Moscardini, L., de Zotti, G., Toffolatti, L., Danese, L. 2005, MNRAS, 358, 869

Nenkova, M., Sirocky, M.M., Nikutta, R., Ivezic, Z., Elitzur, M. 2008, ApJ, 685, 160

Netzer, H., Trakhtenbrot, B. 2007 ApJ, 564, 754

Netzer, H., et al. 2007, ApJ, 666, 806

Netzer, H. 2009, MNRAS, 399, 1907

Noeske, K.G., et al. 2007, ApJ, 660, L43

Norman, C., et al. 2002, ApJ, 571,218

Omont, A., Beelen, A., Bertoldi, F., Cox, P., Carilli, C.L., Priddey, R.S., McMahon, R.G., Isaak, K.G. 2003, A&A, 398, 857

Page, M.J., Stevens, J.A., Mittaz, J.P.D., Carrera, F.J. 2001, Science 294, 2516

Page, M.J., Mittaz, J.P.D., Carrera, F.J. 2001, MNRAS, 325, 575

Page, M.J., Stevens, J.A., Ivison, R.J., Carrera, F.J. 2004, ApJ, 611, L85

Papadopoulos, P.P., Seaquist, E.R. 1999, ApJ, 514, L95

Pier, E.A., Krolik, J.H. 1992, ApJ, 401, 99

Pier, E.A., & Krolik, J.H. 1993, ApJ, 418, 673

Pierce, C.M., et al. 2007, ApJ660, L19

Priddey, R.S., Isaak, K.G., McMahon, R.G., Omont, A. 2003, MNRAS, 339, 1183

Rigopoulou, D., et al. 2009, MNRAS, 400, 1199

Roche, N.D., Dunlop, J., Caputi, K.L., McLure, R., Willott, C.J., Crampton, D. 2006, MNRAS, 370, 74

Rovilos, E., Georgakakis, A., Georgantopoulos, I., Afonso, j., Koekemoer, A.M., Mobasher, B., Goudis, C. 2001, A&A, 466, 119

Rowan-Robinson, M., 1995, MNRAS, 272, 737

Sanders, D.B., Soifer, B.T., Elias, J.H., Madore, B.F., Matthews, K., Neugebauer, G., Scoville, N.Z. 1988, ApJ, 325, 74

Schweitzer, M., et al. 2006, ApJ, 649, 79

Severgnini, P., et al. 2000, A&A, 360, 457

Shapiro, K.L, et al. 2008, ApJ, 682, 231

Silverman, J.D., et al. 2008, ApJ, 675, 1025

Silverman, J.d., et al. 2009, ApJ, 696, 396

Siringo, G., et al. 2009, A&A, 497, 945

Solomon, P.M., VandenBout, P.A. 2005, ARA&A, 43, 677

Steffen, A., et al. 2006, AJ, 131, 2826

Stevens, J.A., Page, M.J., Ivison, R.J., Carrera, F.J., Mittaz, J.P.D., Smail, I., McHardy, I.M. 2005, MNRAS, 360, 610

Sturm, E., Hasinger, G., Lehmann, I., Mainieri, V., Genzel, R., Lehnert, M.D., Lutz, D., Tacconi, L.J. 2006, ApJ, 642, 81

Szokoly, G., et al. 2004, ApJS, 155, 271

Tozzi, P., et al. 2006, A&A, 451, 457

Treister, E., et al. 2009, ApJ, 691, 1713

Trichas, M., Georgakakis, A., Rowan-Robinson, M., Nandra, K., Clements, D., Vaccari, M. 2009, MNRAS, 399, 663

Tueller, J., Mushotzky, R.F., Barthelmy, S., Cannizzo, J.K., Gehrels, N., Markwardt, C.N., Skinner, G.K., Winter, L.M., 2008, ApJ, 681, 113

Waskett, T.J., et al. 2003, MNRAS, 341, 1217

Weiß, A., et al., 2009, ApJ, 707, 1201

Wolf, C., et al. 2004, A&A, 421, 913

Wolf, C., Hildebrandt, H., Taylor, E.N., Meisenheimer, K., 2008, A&A, 491, 933

Zakamska, N.L, Gómez, L., Strauss, M.A., Krolik, J.H. 2008, AJ, 136, 1607

Table 1.   Stacking results for combined CDFS+ECDFS list

Group	N_{Source}	$S_{870\mu m}$ mJy	σ_{map} mJy	$\sigma_{subsample}$ mJy	$S_{870\mu m,residual}$ mJy	L_{IR} $10^{11}L_{\odot}$
(1)	(2)	(3)	(4)	(5)	(6)	(7)
No grouping						
All CDFS & ECDFS	895	0.490	0.044	0.054	0.344	
Grouping by redshift						
z≤1.2	383	0.279	0.066	0.083	0.218	1.15
z>1.2	365	0.637	0.068	0.085	0.445	3.97
z>2	158	0.597	0.106	0.129	0.430	3.79
All z	748	0.453	0.047	0.059	0.328	2.48
No good phot/spec z	147	0.695	0.108	0.134	0.434	

Note. — Col. (1) — Group of X-ray AGN entering the stack.
Col. (2) — Number of sources in stack.
Col. (3) — Weighted mean of 870μm flux densities for stack. Measurements for stacks which are at $< 3\sigma$, hence not significantly detected, are highlighted by italics.
Col. (4) — Standard deviation of the weighted means, obtained by drawing many samples of N_{Source} at random positions from the LABOCA map.
Col. (5) — Standard deviation of the weighted means from drawing many subsamples of N_{Source} from the full N=895 AGN sample.
Col. (6) — Weighted mean of 870μm flux densities for stack on the residual map, obtained by subtracting all individual detections from the original map. For the stacks from the residual map, the corresponding errors σ_{map} and $\sigma_{subsample}$ (not shown) are consistent with each other and $\sim$12% less than σ_{map} for the full map.
Col. (7) — Stacked IR luminosity, from the weighted mean of the luminosities of rest frame T=35K β=1.5 greybodies individually matched to the redshift and 870μm flux of each X-ray AGN. Available only for samples with redshifts for each object.

Table 2.   Stacking results for Tozzi et al. CDFS list

Group (1)	N_{Source} (2)	$S_{870\mu m}$ mJy (3)	σ_{map} mJy (4)	$\sigma_{subsample}$ mJy (5)	$S_{870\mu m,residual}$ mJy (6)	L_{IR} $10^{11}L_\odot$ (7)
No grouping						
All CDFS	302	0.437	0.074	0.094	0.328	2.32
Grouping by redshift						
z≤1	145	0.362	0.109	0.134	0.258	1.47
z>1	157	0.506	0.104	0.128	0.394	3.13
z>2	63	0.779	0.162	0.202	0.561	4.93
Grouping by intrinsic rest frame 2-10keV luminosity						
$L < 10^{42}$erg s^{-1}	48	*0.379*	0.189	0.233	0.289	1.05
$L < 10^{43}$erg s^{-1}	138	0.361	0.111	0.138	0.305	1.52
$L \geq 10^{43}$erg s^{-1}	164	0.500	0.102	0.126	0.348	3.01
$L < 10^{44}$erg s^{-1}	260	0.341	0.086	0.101	0.266	1.71
$L \geq 10^{44}$erg s^{-1}	42	1.036	0.200	0.250	0.718	6.24
Grouping by X-ray obscuring column from spectral fit						
$N_H < 10^{22}$cm^{-2}	114	*0.315*	0.122	0.152	0.280	1.32
$N_H \geq 10^{22}$cm^{-2}	188	0.511	0.095	0.120	0.357	2.94
$N_H < 3 \times 10^{22}$cm^{-2}	169	0.421	0.098	0.115	0.325	2.04
$N_H \geq 3^{22}$cm^{-2}	133	0.458	0.113	0.140	0.333	2.66
$N_H < 10^{23}$cm^{-2}	225	0.416	0.087	0.108	0.310	2.08
$N_H \geq 10^{23}$cm^{-2}	77	0.498	0.149	0.123	0.383	3.01
Sources with $L_{2-10keV} \geq 3\ 10^{43}$erg s^{-1}, grouping by X-ray column						
$N_H < 10^{22}$cm^{-2}	18	*0.072*	0.316	0.378	0.185	0.40
$N_H \geq 10^{22}$cm^{-2}	80	0.641	0.147	0.180	0.427	3.95
$N_H < 10^{23}$cm^{-2}	48	*0.400*	0.189	0.233	0.341	2.42
$N_H \geq 10^{23}$cm^{-2}	50	0.667	0.184	0.226	0.422	4.12
Sources with $L_{2-10keV} \geq 1\ 10^{44}$erg s^{-1} and spectroscopic redshift, grouping by X-ray column						
$N_H < 10^{22}$cm^{-2}	6	*0.433*	0.531	0.653	0.549	2.23
$N_H \geq 10^{22}$cm^{-2}	21	1.390	0.285	0.352	0.858	8.43
$N_H < 10^{23}$cm^{-2}	13	1.098	0.366	0.447	0.860	6.40

Table 2—Continued

Group	$N_{\rm Source}$	$S_{870\mu m}$ mJy	σ_{map} mJy	$\sigma_{subsample}$ mJy	$S_{870\mu m,residual}$ mJy	$L_{\rm IR}$ $10^{11}L_\odot$
(1)	(2)	(3)	(4)	(5)	(6)	(7)
$N_H \geq 10^{23}{\rm cm}^{-2}$	14	1.244	0.346	0.432	0.719	7.57

Sources with $L_{2-10keV} < 3 \times 10^{43}{\rm erg\,s}^{-1}$ and spectro-
scopic redshift, grouping by X-ray column

$N_H < 10^{22}{\rm cm}^{-2}$	96	*0.360*	0.133	0.166	0.298	1.47
$N_H \geq 10^{22}{\rm cm}^{-2}$	108	0.415	0.124	0.156	0.307	2.23

Sources with $L_{0.5-2keV}$ or $L_{2-10keV} \geq 1\ 10^{44}{\rm erg\,s}^{-1}$ and
spectroscopic redshift, grouping by optical spectral type

Type 1 (BLAGN)	10	*0.737*	0.410	0.508	0.743	4.29
Type 2	17	1.436	0.315	0.388	0.815	8.64

Note. — Definition of columns as in Table 1. Stacks measured at $< 3\sigma$, hence
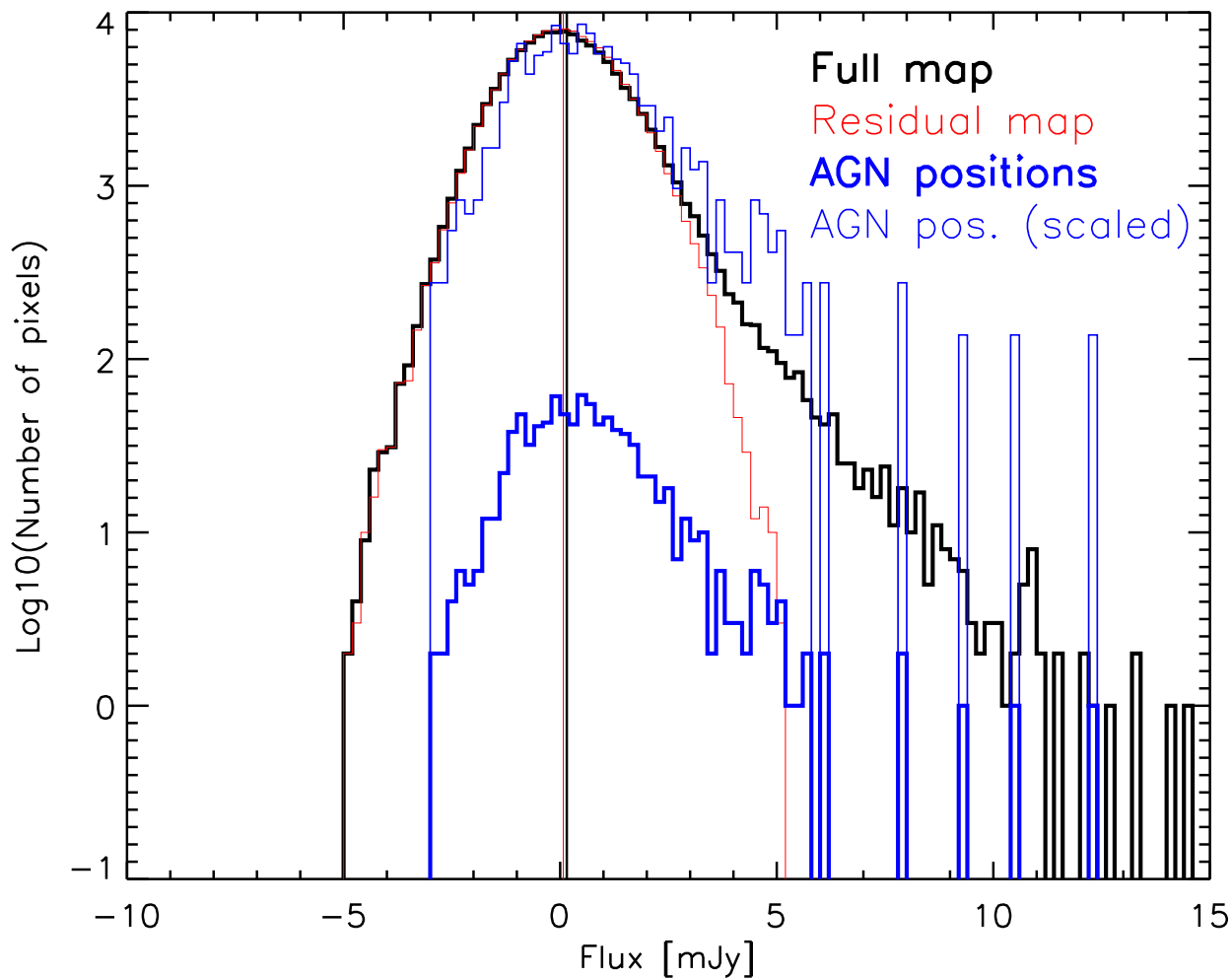not significantly detected, are highlighted by italics.

Fig. 1.— Pixel flux histograms for the roughly 80% of the LABOCA 870μm map of the ECDFS with RMS less or equal 1.5 times the minimum noise of 1.07mJy. The black thick histogram represents the full map, the red thin histogram the residual map after subtraction of detected sources (Weiß et al. 2009). Vertical lines indicate the mean flux of this region in the respective map. The blue thick histogram shows the flux distribution at the positions of the combined sample of 895 CDFS and ECDFS AGN. The blue thin histogram shows for easy comparison this AGN histogram scaled to the number of map pixels.
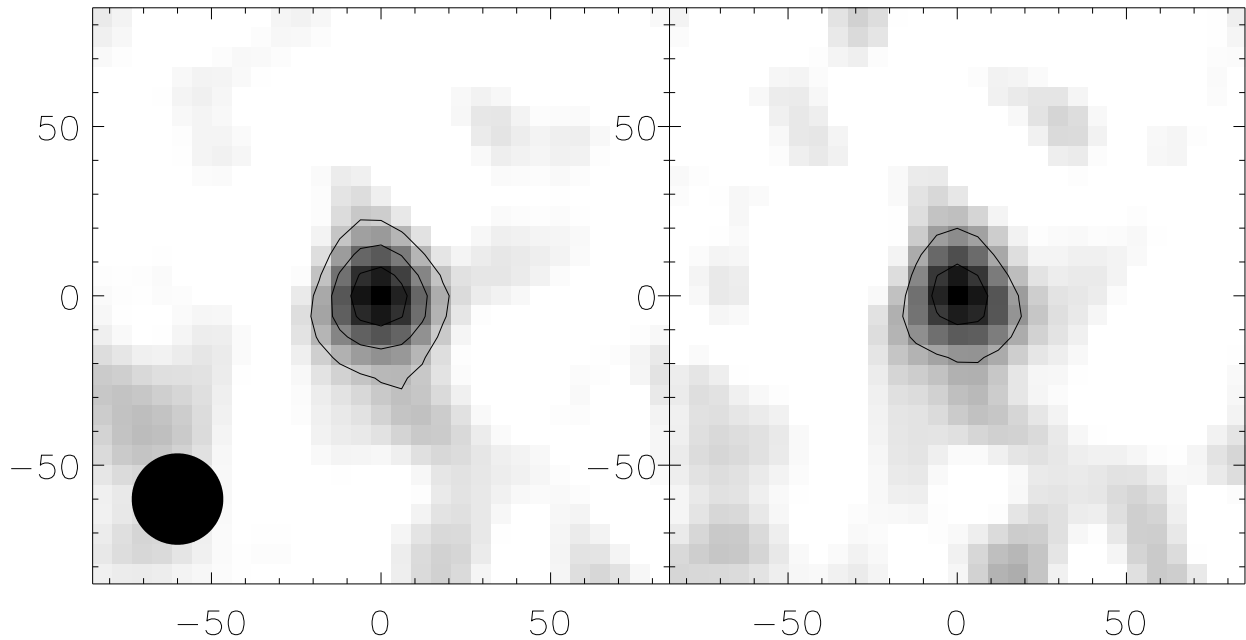
Fig. 2.— Stamps showing the coadded LABOCA submm signal for all 895 CDFS and ECDFS X-ray sources in our combined list. Left: Obtained using the total LABOCA flux map. The 27″ FWHM beamsize of the LABOCA map is shown for comparison in the bottom left. Right: Obtained using the residual map after subtraction of all sources individually detected above 3.7σ. The spatial scale is in arcseconds relative to the expected nominal center of the stacked beam. Contours are shown at 3, 6, 9 times the full stack noise of 0.044mJy. The greyscale of the images runs from zero to the respective peak.
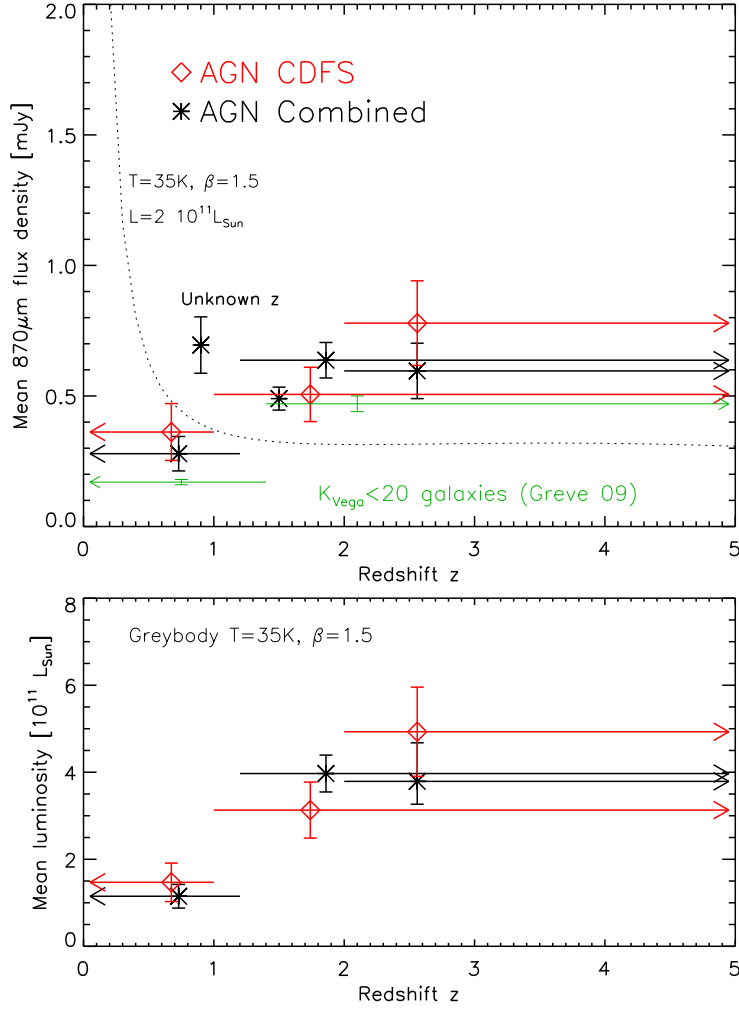
Fig. 3.— Top panel: X-ray selected AGN from the CDFS and ECDFS show an increasing trend of mean submm flux density with redshift. As in similar diagrams below, horizontal bars or arrows indicate the parameter range covered by a subsample, while vertical error bars indicate the 1σ errors of the mean flux for this subsample. The symbols are placed at the median of the quantity on the abscissa for the respective bin - here redshift. The asterisk without redshift range indicates the mean flux of the entire combined sample. Results are shown separately for CDFS AGN only, and for the combined sample of CDFS and ECDFS AGN. Results for ECDFS sources without reliable redshift are shown at an arbitrary z, most likely these contain a significant fraction of presently unidentified high redshift sources. The mean submm fluxes of (predominantly non-AGN) K<20 galaxies are added for comparison (Greve et al. 2009, also based on LABOCA data). We also illustrate the submm flux expected from a greybody of given luminosity at different redshifts (dashed curve). Bottom panel: Results from stacking the IR luminosities of greybodies fitted to the redshift and map flux of each source.
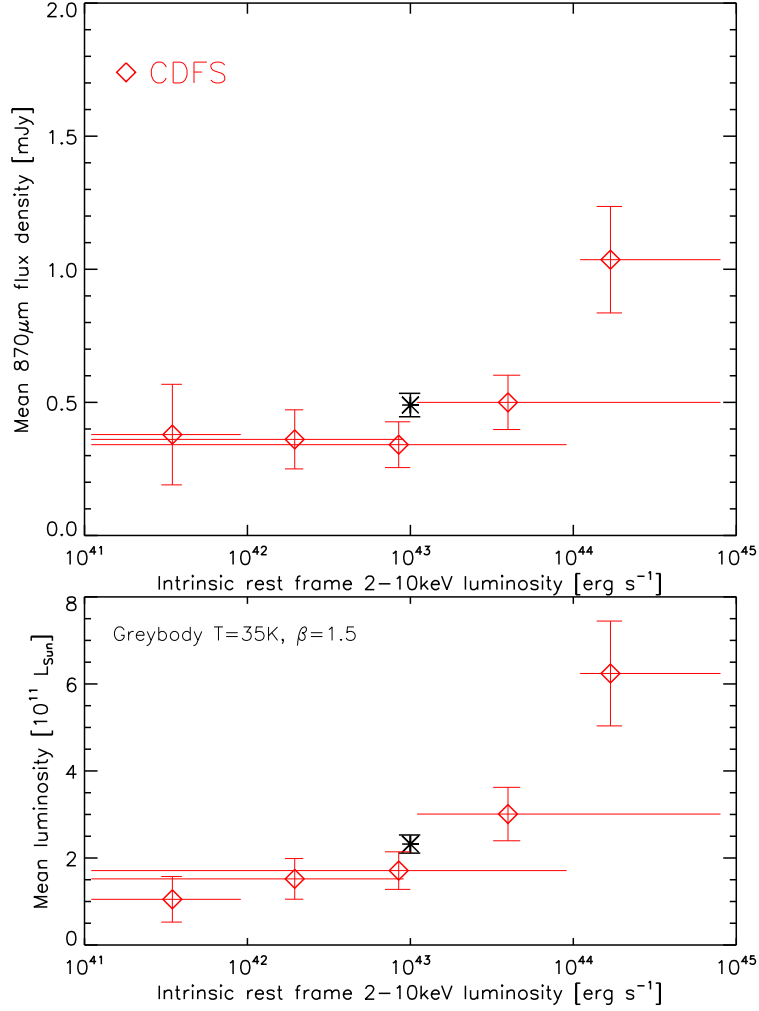
Fig. 4.— Top panel: Mean submm flux density as a function of intrinsic rest frame 2-10keV luminosity of the AGN. The asterisk indicates the mean submm flux of the entire combined sample. The mean submm flux rises clearly above $L_{2-10keV} = 10^{44}$erg s^{-1}. These highest luminosities are also the sole driver of the flux increase in the wider $L_{2-10keV} = 10^{43}$erg s^{-1} bin. Bottom panel: Results from stacking the IR luminosities of greybodies fitted to the redshift and map flux of each source.
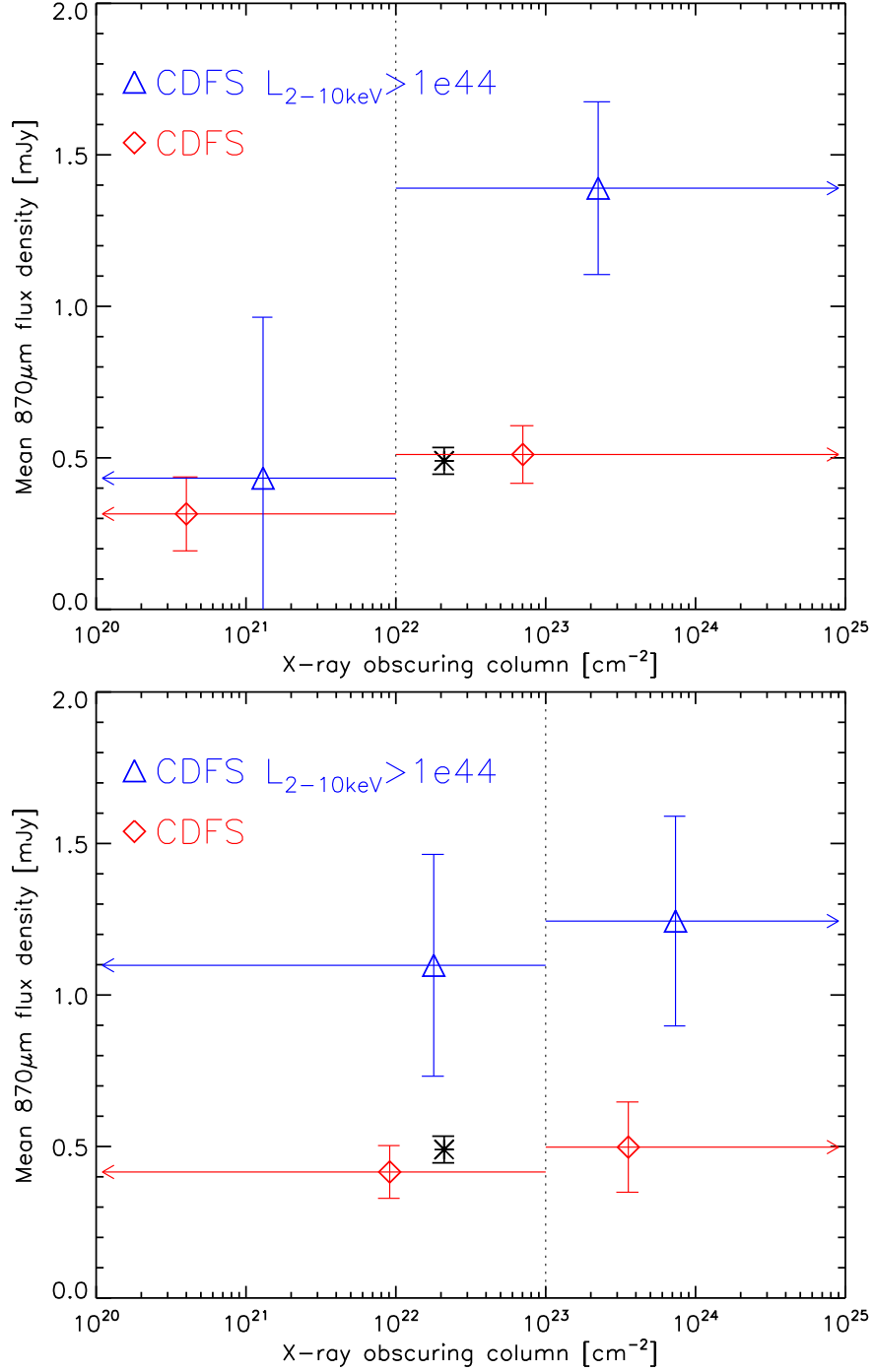
Fig. 5.— Trends of mean submm flux density with AGN X-ray obscuring column density. Top panel: Sample split at $N_H = 10^{22} \mathrm{cm}^{-2}$, as indicated by the dotted line. Bottom panel: Sample split at $N_H = 10^{23} \mathrm{cm}^{-2}$. The asterisk shows the mean flux of the entire combined sample. We show results for the full CDFS sample, with no indication for a trend with N_H, and for the the most X-ray luminous CDFS sources with good redshifts. From the top panel, these may be more submm luminous above $N_H = 10^{22} \mathrm{cm}^{-2}$ compared to below, but the difference is not significant in our sample.
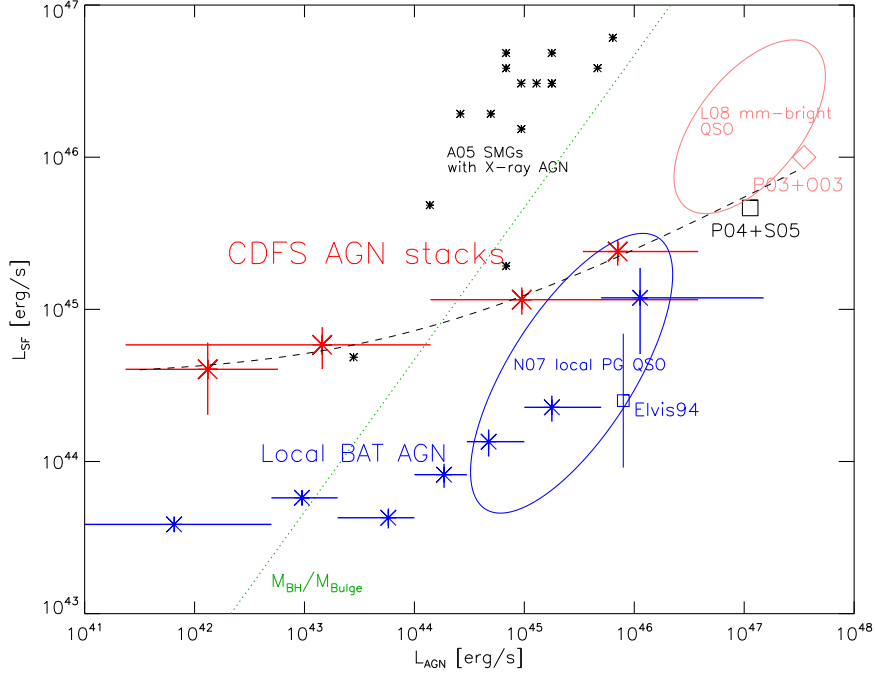
Fig. 6.— AGN luminosities and star forming far-infrared luminosities for high redshift and local AGN. Moderate luminosity AGN have host star formation rather independent of AGN luminosity, but at a level rising with redshift. For high AGN luminosity, AGN luminosity and host star formation correlate. Red asterisks represent the four CDFS AGN stacks grouped by intrinsic 2-10keV X-ray luminosity, as also shown in Fig.4 and Table 2. The four stacks are for $L_{2-10keV} < 10^{42}$, $< 10^{43}$, $> 10^{43}$ and $> 10^{44}$erg s^{-1} (see also the horizontal bars indicating the range of AGN luminosities entering) and are plotted at the median AGN luminosity of the sources in each stack. The diagonal dotted green line indicates the relation for a continuous host and black hole growth, reflecting the local universe relation between black hole mass and bulge mass. The black square represents the combined X-ray obscured and unobscured samples of more luminous X-ray AGN from Page et al. (2004) and Stevens et al. (2005) [P04, S05], see also Section 3. AGN and star formation luminosities have been obtained analogously to the CDFS stacks. The pink ellipse indicates the location in such a diagram of mm-bright and optically very luminous high-z QSOs studied by Lutz et al. (2008) [L08]. The pink diamond reflects the suggested median location of the parent population of these luminous high-z QSOs including mm-faint ones, as discussed in Lutz et al. (2008) and based on the surveys of Priddey et al. (2003) and Omont et al. (2003) [P03, O03]. The dashed line is a simple constant plus power law relation between AGN and star forming luminosity approximating the high redshift AGN. We also include local universe (z< 0.3) AGN, the blue ellipse representing local PG QSOs studied by Netzer et al. (2007) and the blue asterisks stacks of local hard X-ray selected AGN based on *Swift*-BAT and *IRAS* data (Section 3.3). The blue square represents the Elvis et al. (1994) QSO sample at its median AGN luminosity converted to our cosmology, with the error bar indicating the 1σ variation in FIR/optical (star formation/AGN) flux ratio of objects in that sample. Submillimeter galaxies with weak X-ray AGN (Alexander et al. 2005a) are shown for comparison.